



1 Overview: Fusion of Radar Polarimetry and Numerical Atmospheric 2 Modelling Towards an Improved Understanding of Cloud and 3 Precipitation Processes

4 Silke Trömel^{1,2}, Clemens Simmer¹, Ulrich Blahak³, Armin Blanke¹, Florian Ewald⁴, Michael Frech⁵,
5 Mathias Gergely⁵, Martin Hagen⁴, Sabine Hörnig⁶, Tijana Janjic⁷, Heike Kalesse⁶, Stefan Kneifel⁸,
6 Christoph Knot^{7,9}, Jana Mendrok³, Manuel Moser^{10,4}, Gregor Möller⁷, Kai Mühlbauer¹, Alexander
7 Myagkov¹¹, Velibor Pejic¹, Patric Seifert¹², Prabhakar Shrestha¹, Audrey Teisseire¹², Leonie von Terzi⁸,
8 Eleni Tetoni⁴, Teresa Vogl⁶, Christiane Voigt^{10,4}, Yuefei Zeng⁷, Tobias Zinner⁷, Johannes Quaas⁶

9 ¹Institute for Geosciences, Department of Meteorology, University of Bonn, Bonn, 53121, Germany

10 ²Laboratory for Clouds and Precipitation Exploration, Geoverbund ABC/J, Bonn, 53121, Germany

11 ³Deutscher Wetterdienst (DWD), Offenbach, 63067, Germany

12 ⁴Institute for Physics of the Atmosphere, DLR, Oberpfaffenhofen, 82234, Germany

13 ⁵Deutscher Wetterdienst (DWD), Observatorium Hohenpeißenberg, Hohenpeißenberg, 82383, Germany

14 ⁶Institute for Meteorology, Universität Leipzig, Leipzig, 04103, Germany

15 ⁷Meteorological Institute Munich, Ludwig-Maximilians-Universität München, 80333, Germany

16 ⁸Institute of Geophysics and Meteorology, University of Cologne, 50969, Germany

17 ⁹Faculty of Medicine, University of Augsburg, Augsburg, 86159 Germany

18 ¹⁰Institute for Physics of the Atmosphere, University Mainz, Mainz, 55099, Germany

19 ¹¹Radiometer Physics GmbH, Meckenheim, 53340, Germany

20 ¹²Leibniz Institute for Tropospheric Research (TROPOS), 04318 Leipzig, Germany

21
22
23 *Correspondence to:* Silke Trömel (silke.troemel@uni-bonn.de)

24 **Abstract.** Cloud and precipitation processes are still the main source of uncertainties in numerical weather prediction and
25 climate change projections. The Priority Program “Polarimetric Radar Observations meet Atmospheric Modelling (PROM)“,
26 funded by the German Research Foundation (Deutsche Forschungsgemeinschaft, DFG), is guided by the hypothesis, that many
27 uncertainties relate to the lack of observations suitable to challenge the representation of cloud and precipitation processes in
28 atmospheric models. Such observations can, however, nowadays be provided e.g. by the recently installed dual-polarization C
29 band weather radar network of the German national meteorological service in synergy with cloud radars and other instruments
30 at German supersites and similar national networks increasingly available worldwide. While polarimetric radars potentially
31 provide valuable in-cloud information e.g. on hydrometeor type, quantity, and microphysical cloud and precipitation processes,
32 and atmospheric models employ increasingly higher moment microphysical modules, still considerable knowledge gaps exist
33 in the interpretation of the observations and large uncertainties in the optimal microphysics model process formulations. PROM



34 is a coordinated interdisciplinary effort to intensify the use of polarimetric radar observations in data assimilation, which
35 requires a thorough evaluation and improvement of parametrizations of moist processes in atmospheric models. As an
36 overview article of the inter-journal special issue “Fusion of radar polarimetry and numerical atmospheric modelling towards
37 an improved understanding of cloud and precipitation processes”, it outlines the knowledge achieved in PROM during the past
38 two years and gives perspectives for the next four years.

39 **1 Introduction and Objectives of the priority program**

40 The main source of uncertainty in numerical weather prediction (NWP) and climate change projections are cloud and
41 precipitation processes. A major part of these uncertainties can be attributed to missing observations suitable to challenge the
42 representation of cloud and precipitation processes employed in atmospheric models. Since several years a wealth of new
43 information on precipitation microphysics and generating processes can be gained from observations from polarimetric
44 weather radars and their synergistic analysis at different frequencies. The dual-polarization upgrade of the United States
45 National Weather Service (NWS) S-Band Weather Surveillance Radar 1988 Doppler (WSR-88D) network was completed in
46 2013. Germany finished upgrading its C-band network to polarimetry in 2015 in parallel to other European countries. Together
47 with measurements from cloud radars and other instrumentation available at supersites and research institutions their synergetic
48 exploitation enables for the first time a thorough evaluation and potential improvement of current microphysical
49 parameterizations based on detailed multi-frequency remote-sensing observations. Data assimilation merges observations and
50 models for state estimation as a prerequisite for prediction and can be considered as a smart interpolation between observations
51 while exploiting the physical consistency of atmospheric models as mathematical constraints.

52 Considerable knowledge gaps still exist, however, both in radar polarimetry and atmospheric models, which still impede the
53 full exploitation of the triangle radar polarimetry – atmospheric models – data assimilation and called for a coordinated
54 interdisciplinary effort. The German Research Foundation (Deutsche Forschungsgemeinschaft, DFG) responded to this call
55 and established the Priority Program „Polarimetric Radar Observations meet Atmospheric Modelling (PROM)“; its first 3-
56 year funding period started 2019, which will be followed by a second funding period starting in 2022. PROM will exploit the
57 synergy of polarimetric radar observations and state-of-the-art atmospheric models to better understand moist processes in the
58 atmosphere, and to improve their representation in climate- and weather prediction models. The overarching goal is to extend
59 our scientific understanding at the verges of the three disciplines radar polarimetry – atmospheric models – data assimilation
60 for better predictions of precipitating cloud systems. To approach this goal the initiators of PROM at the Universities of Bonn
61 and Leipzig in Germany identified the following five objectives (see also Trömel et al. 2018):



- 62 1) Exploitation of radar polarimetry for quantitative process detection in precipitating clouds and for model evaluation,
- 63 2) Improvement of cloud and precipitation schemes in atmospheric models based on process fingerprints detectable in
64 polarimetric observations,
- 65 3) Monitoring of the energy budget evolution due to phase changes in the cloudy, precipitating atmosphere for a better
66 understanding of its dynamics,
- 67 4) Generation of precipitation system analyses by assimilation of polarimetric radar observations into atmospheric models for
68 weather forecasting, and
- 69 5) Radar-based detection of the initiation of convection for the improvement of thunderstorm prediction.

70 In the first funding period, 14 projects (see <https://www2.meteo.uni-bonn.de/spp2115>) distributed over Germany contribute to
71 at least one of these objectives. In most projects, a radar meteorologist works together with a modeller in order to successfully
72 combine expert knowledge from both research fields. This overview article of the ACP/AMT/GMD inter-journal special issue
73 entitled “Fusion of radar polarimetry and numerical atmospheric modelling towards an improved understanding of cloud and
74 precipitation processes” outlines methodologies developed and results achieved from a selection of the projects during the past
75 two years and provides overall perspectives for the next four years. The paper is organized as follows: Section 2 explains
76 prevailing challenges in the representation of clouds in atmospheric models, while Sect. 3 provides methodologies to extend
77 our insight in the microphysics of clouds and precipitation by exploiting radar polarimetry. Section 4 addresses the fusion of
78 both disciplines - numerical modelling and radar polarimetry - via model evaluation either in radar observation space using
79 forward operators or using microphysical retrievals. First conclusions for improved model parameterizations and for a better
80 representation of model uncertainty in the process of radar data assimilation are drawn. Section 5 provides a summary and
81 perspectives for the following years.

82 **2 Representation of clouds in atmospheric models**

83 The representation of cloud- and precipitation processes in atmospheric models is a central challenge for NWP and climate
84 projections (e.g., Boucher et al., 2013; Bauer et al., 2015); they also impact offline hydrological models by significantly
85 modulating the distribution of incoming solar radiation and precipitation and affecting the simulated hydrological processes
86 such as evapotranspiration, runoff, and groundwater depths (e.g., Shrestha 2021). While the primitive equations provide a solid
87 theoretical basis for atmospheric model dynamics, the key diabatic processes that drive energetics and thus circulation, are
88 hardly resolved. These are the cloud microphysical processes acting at scales of micrometres and turbulent processes ranging
89 from several to hundreds of meters. While significant progress has been achieved by high-resolution modelling at the coarser
90 end of this range (e.g., Heinze et al., 2017; Stevens et al., 2020), the intricate and complex microphysical processes will still
91 require parameterizations in any dynamic atmospheric model down to the scale of direct numerical simulations (e.g., Mellado
92 et al., 2009).



93 A key uncertainty in weather prediction and climate modelling results from the still rudimentary representation of moist
94 processes and the diabatic heating/cooling they induce due to latent heat and their interaction with radiation. The generation
95 and interpretation of past and future climate states has in addition to consider changes in microphysical processes due to
96 anthropogenic aerosol acting e.g. as cloud condensation nuclei and ice nucleating particles. For short-term weather prediction,
97 the location and evolution of convective events with lifetimes of hours or less are particularly challenging, while relatively
98 slow moving and frontal systems with lifetimes of days show reasonable predictability (Alifieri et al., 2012). High-resolution
99 simulations and observations of fronts point at their composition of small-scale filament-type short-lived convective features,
100 but their importance for the system evolution (and predictability) is not yet fully understood.

101 Atmospheric modelling in Germany has recently seen substantial advances both in terms of cloud-resolving simulations in
102 NWP mode and in the implementation of ice and mixed-phase precipitation formation processes. Traditionally, different model
103 systems were used for NWP and climate modelling, which were also both heavily used in academic research. Research with
104 the ECHAM model family originating from the NWP model of the European Centre for Medium-Range Weather Forecasts
105 (ECMWF) focused on long-term climate integrations at horizontal resolutions of the order of 100 km (Stevens et al., 2013),
106 and the COSMO model operated at horizontal resolutions down to 2.8 km was used for NWP and reanalysis studies. Both
107 model families are currently replaced by the ICOSahedral Nonhydrostatic (ICON) modelling framework (Zängl et al., 2015)
108 jointly developed by Max-Planck Institute for Meteorology and the German national meteorological service (Deutscher
109 Wetterdienst, DWD). Its climate version (the ICON general circulation model, ICON GCM) inherited its physics package
110 from the ECHAM model, and the NWP version incorporated the one from the COSMO model. A third version largely based
111 on the COSMO physics package was developed for higher resolutions (Dipankar et al., 2015) and employs a large-eddy
112 turbulence scheme (ICON-LEM). The latter is able to operate on large domains (Heinze et al., 2017; Stevens et al., 2020) and
113 includes aerosol-cloud interactions (Costa-Surós et al., 2020). In PROM primarily the ICON variants are used.

114 In most atmospheric models, cloud and precipitation microphysical processes are represented by bulk microphysical schemes
115 that distinguish between different hydrometeor classes and include their specific masses as prognostic variables while their
116 size distributions are parameterized. Computationally much more demanding are so-called spectral-bin microphysics schemes
117 (Khain et al., 2015), which evolve cloud- and precipitation particle size distributions discretized into size-interval bins. An
118 example is the Hebrew University cloud model created by Khain et al. (2005) that treats both liquid and much more intricate
119 ice crystal distributions. The model is employed by some of the PROM projects in addition to the liquid-only bin-microphysics
120 model by Simmel et al. (2015) extended by the ice phase based on the scheme by Hashino and Tripoli (2007). For the simulation
121 of the evolution of specific air volumes a Lagrangian particle model (McSnow; Brdar and Seifert, 2018) is used in PROM, that
122 models ice and mixed-phase microphysical processes such as depositional growth, aggregation, riming, secondary ice
123 generation, and melting closer to the real processes than bulk formulations. Microphysical processes including radiation-
124 particle interactions obviously depend on particle shape; thus the evolution of shapes in particle models – and their signatures



125 in radar observations – is instrumental for a full understanding and adequate representation of the microphysical processes in
126 models. Advanced microphysical parameterizations such as spectral-bin or Lagrangian particle schemes are relevant for cloud-
127 resolving models and exploited for the development and improvement of bulk parameterizations. Scientific questions about
128 global climate necessitate long model integrations and thus coarse spatial resolutions which require parameterizations of the
129 spatial cloud variability; here PROM builds on assumptions employed in the global ICON model (ICON GCM) to predict
130 fractional cloudiness (e.g., Quaas, 2012).

131 **3 Observational insights from polarimetric radar observations and remaining challenges**

132 DWD operates 17 state-of-the-art polarimetric Doppler C-band weather radars which provide a 3-D sampling of precipitation
133 processes every five minutes. Together with the Doppler information from those systems, radar data are the backbone for
134 precipitation and nowcasting products for all meteorological services. Although precipitation monitoring is still the most
135 widespread application of weather radars, their upgrade to polarimetry worldwide not only improve precipitation estimates,
136 their observations are also increasingly exploited for the evaluation and improvement of the representation of cloud- and
137 precipitation processes in atmospheric models. Additional observations from cloud radars nowadays available at so-called
138 supersites (in Germany e.g. the Jülich Observatory for Cloud Evolution – Core Facility; JOYCE-cf; Löhnert et al. 2015;
139 <http://www.cpex-lab.de>), universities, and research facilities (e.g. the Leipzig Aerosol and Cloud Remote Observations
140 System; LACROS; Bühl et al., 2013) open extended opportunities to inform and improve atmospheric models. The use of
141 shorter wavelengths of cloud radars shifts the sensitivity of the observations towards smaller particles and partly increases the
142 strength of the received polarimetric signals (e.g. K_{DP} – the phase change between horizontal and vertical polarization per
143 distance called specific differential change – scales with λ^{-1}), which allows for more detailed studies of ice and cloud
144 microphysics. Polarimetric and multi-frequency radar observations allow even more to zoom in microphysical processes and
145 provide a great data base for model evaluation, the improvement of microphysical parameterizations, and data assimilation,
146 and thus have the potential to significantly improve both weather forecasts and climate predictions.

147 **3.1 Multi-frequency and spectral polarimetry for ice and cloud microphysics**

148 The PROM-project *Understanding Ice Microphysical Processes by combining multi-frequency and spectral Radar*
149 *polarImetry aNd super-parTicle modelling (IMPRINT)* aims at improving our ice microphysical process understanding by
150 using multi-frequency spectral radar polarimetric observations. Spectral polarimetry exploits in particular the different terminal
151 velocities of hydrometeor types to quantify their contributions to the total measured polarimetric quantity; e.g. the strong
152 polarimetric signals generated by small ice particles can be separated from the weak polarimetric contribution of large
153 aggregates to the total measured differential reflectivity Z_{DR} . The combination of spectral polarimetric with multi-frequency
154 radar observations allows for the investigation of the evolution of particle sizes in detail. A common observable is the dual
155 wavelength ratio, which is defined as the logarithmic difference of the effective reflectivity Z_e at two frequencies. If ice



156 particles transition from the Rayleigh scattering to the non-Rayleigh scattering regime at the higher frequencies, the dual-
157 wavelength reflectance ratio (DWR) increases and thus indicates an increase of the mean size of the particle size distribution
158 (e.g. Ori et al., 2020). Fig. 1a shows the DWR during snowfall at the ground observed at Ka and W band for 2019-01-22 over
159 the “Jülich Observatory for Cloud Evolution – Core Facility” (JOYCE-cf). At about 15 UTC, the DWR-KaW strongly
160 increases in about 2300 m height indicating the onset of strong aggregation. While DWR is sensitive to large aggregates, high
161 Z_{DR} (the difference between horizontal and vertical radar reflectivity) indicates asymmetric particles (in case of frozen
162 precipitation it signals small ice crystals). Since Z_{DR} is an integral signal of the present particle size distribution (PSD), it is
163 dominated by the larger aggregates and thus decreases at the height level where DWR-KaW starts to rise (Fig. 1b). K_{DP} also
164 starts rising at this level (Fig. 1c), which may indicate secondary ice production. The spectrally resolved DWR-KaW and Z_{DR}
165 (sZ_{DR}) at 15 UTC are shown in Figs 1d-e for more detailed insights. Enhanced DWR-KaW on the left side of the spectrum
166 indicates aggregates already present above -15°C reaching maximum sizes at around -10°C . The width of the DWR-KaW
167 spectrum starts to increase rapidly already at around -17°C resulting in a secondary spectral mode at -15°C , and sZ_{DR} reaches
168 values of up to 3 dB for the slow falling particles. A possible interpretation of the bimodal DWR spectrum at increased sZ_{DR}
169 and K_{DP} is the fragmentation of delicate ice crystal structures, which have been found in laboratory studies to evolve close to
170 -17°C (Takahashi et al., 1995; Takahashi 2014). The fragmentation signal might not only relate to single crystals but could
171 also be caused by dendritic structures growing at the surface of aggregates similar to the growth structures found on ice spheres
172 at similar temperatures in the laboratory study by Takahashi (1993).

173

174 The PROM-project *Investigation of the initiation of convection and the evolution of precipitation using simulations and*
175 *polarimetric radar observations at C- and Ka-band (IcePolCka)* combines in a novel approach the observations of the C-
176 band POLDIRAD at DLR, Oberpfaffenhofen, with those of the Ka-band miraMACS at LMU, Munich, to study convective
177 cells with a focus on ice particle growth and its role in precipitation formation. Coordinated Range-Height-Indicator (RHI,
178 varying elevation at constant azimuth) scans provide simultaneous measurements of the respective DWR (Fig. 2a) and Z_{DR}
179 (Fig. 2b) along the 23 km long cross-section between the two radar instruments while convective cells are tracked. The
180 deviation from Rayleigh scattering with increasing ice crystal size is used to distinguish regions with larger ice crystals formed
181 by riming or aggregation from regions with depositional growth indicated by enhanced DWR of reflectivities at the longer and
182 shorter wavelength. While this technique provides valuable information on ice crystal size, the unknown ice crystal shape still
183 leads to ambiguities in the identification and retrieval of ice microphysics. Here, simultaneous polarimetric measurements, like
184 Z_{DR} , help to narrow down the average asphericity of ice crystals and reduce ambiguities in ice crystal size and ice water content.
185 The measurements are compared with scattering calculations to identify ice crystal size and asphericity, which enters a retrieval
186 algorithm currently in development. The polarimetric, multi-wavelength measurements are also used as a benchmark for
187 precipitation formation in NWP models. A nested WRF setup covering the overlap area of both radars is used to simulate
188 convective events with microphysical schemes of varying complexity. The Cloud-resolving model Radar SIMulator (CR-SIM;
189 Oue et al., 2020), a development outside PROM, is applied to produce synthetic radar observations, like the DWR (Fig. 2c)



190 and Z_{DR} (Fig. 2d). *IcePolCKa* has collected a 2-year dataset, which is currently used to analyze the performance of different
191 microphysical schemes on a sound statistical basis. E.g. Fig. 2 illustrates that the predicted particle properties (P3) scheme
192 (Morrison and Milbrandt, 2015) is able to produce DWR features of similar magnitude and variability compared to the
193 observations while a realistic ice particle asphericity is still missing.

194

195 The PROM-project *A seamless column of the precipitation process from mixed-phase clouds employing data from a*
196 *polarimetric C-band radar, a microrain radar and disdrometers (HydroColumn)* characterizes precipitation processes inside
197 a vertical atmospheric column by combining polarimetric Doppler weather radar observations with co-located measurements
198 from micro-rain radars, disdrometers and in-situ measurements, and by relating these high-resolution observations to the large-
199 scale atmospheric thermodynamics derived from NWP models. To date spectral analyses are mostly performed with cloud
200 radars operating at shorter wavelengths (see previous paragraphs), but their applicability to the national C-band radar network
201 offers prospects for operational area-wide applications, e.g. the identification of dominant precipitation particle growth process
202 such as aggregation or riming. *HydroColumn* plans to provide the proof of concept that Doppler spectra measured at C-band
203 provide beneficial microphysical process information. As an example, Fig. 3 shows quasi-vertical profiles (QVPs; Trömel et
204 al., 2014; Ryzhkov et al., 2016) of polarimetric variables and Doppler spectra from birdbath scans for a stratiform precipitation
205 event monitored with the Hohenpeißenberg C-band research radar (47.8014N, 11.0097E) of DWD together with in-situ particle
206 images obtained by the Falcon research aircraft from the German Aerospace Center (DLR) during the BLUESKY campaign
207 (Voigt et al., 2021) within the *POLICE* project (Sect. 3.2). In-situ measurements have been performed with the Cloud, Aerosol
208 and Precipitation Probe CAPS (Kleine et al., 2018) integrated in a wing station on the Falcon flying within a horizontal distance
209 of about 20 km from the radar site and within about ± 15 min of the radar measurements. The dendritic growth layer (DGL)
210 centered around -15 °C is characterized by Z_{DR} maxima of ~ 1 dB and K_{DP} of ~ 0.2 ° km⁻¹, and a strong Z_H -increase towards
211 lower levels (Fig. 3a). Particle images collected at temperatures colder than about -15 °C indicate mostly small irregular ice
212 particles with the number of larger particles increasing toward -15 °C (see levels L1 and L2 in Fig. 3c), and further down also
213 reveal dendrites and plates (L3, L4). In general, aggregation and riming become highly effective particle growth mechanisms
214 at temperatures around -7 °C (Libbrecht 2005) resulting in a reduction of Z_{DR} (Fig. 3a). In this specific case study, the absence
215 of secondary spectral modes in the Doppler spectra at C-band combined with relatively slow mean Doppler velocities above
216 the melting layer suggests aggregation instead of riming as the dominant growth process (Fig. 3b). This is confirmed by in-
217 situ images showing irregular 3-D structures of occasionally very large size while no large supercooled liquid droplets required
218 for significant riming were recorded (L6).

219

220 3.2. Anthropogenic modifications of precipitation microphysics

221 The PROM-project *Polarimetry Influenced by CCN and INP in Cyprus and Chile (PICNICC)* thrives to improve our
222 understanding of aerosol effects on microphysical growth processes in mixed-phase clouds. *PICNICC* exploits unique remote-



223 sensing datasets from the LACROS suite extended with ground-based remote sensing instruments of Leipzig University,
224 Universidad de Magallanes (Punta Arenas), and Cyprus University of Technology (Limassol). Thus, dual-frequency
225 polarimetric radar observations from the polluted, aerosol-burden Northern and from the clean, pristine Southern hemisphere
226 can be contrasted for microphysical process studies. Since higher ice crystal concentrations favour aggregation, the latter is
227 expected to be more frequent for high aerosol loads and accordingly higher ice nucleating particle (INP) concentrations, while
228 riming should prevail when supercooled liquid layers are sustained due to a scarcity of INP. Evaluating this hypothesis requires
229 the distinction between aggregation and riming processes in mixed-phase cloud systems. Fig. 4 demonstrates for 30 August
230 2019, when a deep mixed-phase cloud system passed the site, the capability of the LACROS suite when combined with a 94-
231 GHz Doppler radar at the low-aerosol site in Punta Arenas (53°S, 71°W), Chile, to distinguish between aggregates and rimed
232 particles. The pattern of the 94-GHz radar reflectivity factor (Z_e , Fig. 4a) underlines the complex structure of the system. The
233 height spectrogram of vertical-stare 94-GHz slanted linear depolarization ratio (SLDR, Fig. 4 e) from 08:30 UTC exhibits
234 regions of changing shape signatures and multi-modality in the cloud radar Doppler spectra, where multiple hydrometeor
235 populations coexist. From the RHI scans of SLDR and the co-cross correlation coefficient of horizontal and vertically polarized
236 channels in the slanted basis ρ_{hv} at 35-GHz (Fig. 4 b, c) the polarizability ratio ξ_e (Myagkov et al., 2016) is obtained (Fig. 4d),
237 which allows to estimate a density-weighted hydrometeor shape. For the purpose of shape classification, SLDR is more suited
238 compared to LDR. By slanting the polarization basis by 45°, the returned LDR signatures are much less sensitive to the canting
239 angle distribution of the targets, especially at low elevation angles (Myagkov et al., 2016). The polarimetric RHI scans and the
240 Doppler spectra data allow to retrieve the vertical profile of the hydrometeors: Columnar-shaped bullet rosettes are formed
241 between 2.5 km height and cloud top as indicated in the RHI scans by an elevation-constant SLDR (Fig. 4b) and an increase
242 of ρ_{hv} with decreasing elevation (Fig. 4c). ξ_e is around 1.3 (Fig. 4d), which is characteristic for slightly columnar crystals.
243 Already at around 3 km height (-15 to -20°C) a decreasing elevation-dependence of ρ_{hv} suggests a more random particle
244 orientation; here the W-band SLDR spectra (Fig. 4e) show reduced values, likely due to the co-existence of dendritic ice
245 crystals, which are formed preferably in this temperature range and cause low SLDR at vertical-stare. The co-location of
246 dendrites and columnar crystals can be explained by either splintering of the arms of the dendritic crystals or a mixing of
247 locally produced dendrites with columnar crystals from higher up, or both. At heights below 2.5 km, ξ_e decreases toward unity,
248 indicating the growth of isometric particles. Also the vertical-stare W-Band SLDR slowly decreases toward the cloud base,
249 while fall velocities increase (Fig. 4e). Both features are characteristic for riming, which is corroborated by co-located lidar
250 observation detecting liquid water in the cloud-base region (not shown).

251

252 The PROM-project *Investigating the impact of Land-use and land-cover change on Aerosol-Cloud-precipitation*
253 *interactions using Polarimetric Radar retrievals (ILACPR)* will provide new insights on the impact of anthropogenic land-
254 use and land-cover changes on precipitating cloud structure and its dynamics. A co-analysis of polarimetric radar observations
255 and model simulations is used to investigate interactions between land-aerosol-cloud-precipitation processes, which will allow
256 to interrogate the effects of anthropogenic interventions on precipitation generating processes and the capabilities of numerical



257 models to reproduce them. The Terrestrial Systems Modeling Platform (TSMP; Shrestha et al., 2014; Gasper et al., 2014)
258 developed by the DFG-funded Transregional Research Center TR32 (Simmer et al., 2015) was used to simulate a hailstorm
259 observed on 5 July 2015 with the polarimetric X-band radar (BoXPol, e.g. Diederich et al., 2015a,b) passing the city of Bonn,
260 Germany. Sensitivity simulations were conducted using large-scale aerosol perturbations and different land-cover types
261 reflecting actual, reduced and enhanced human disturbances. While the differences in modelled precipitation in response to
262 the prescribed forcing were below 5 %, the micro- and macrophysical pathways were found to differ, acting as a buffered
263 system to the prescribed forcings (Stevens and Feingold, 2009; Seifert and Beheng, 2012). Fig. 5 shows vertical cross-section
264 measured with BoXPol together with simulated Z_H and Z_{DR} for the TSMP simulations with actual land-cover but perturbed
265 condensation nuclei (CN) and ice nucleating particle (INP) concentrations. The Bonn Polarimetric Radar forward Operator,
266 B-PRO, (Xie et al., 2021; Xie et al., 2016; Heinze et al., 2017) based on an early version of EMVORADO (Zeng et al., 2016)
267 and further developed within the *Operation Hydrometeors* project jointly with the polarimetric version of EMVORADO
268 (Mendrok et al., 2021; see also Sec. 3.1) has been applied to generate the synthetic variables. The vertical cross sections are
269 compared at different times marked by the vertical grey bars in the time series of Convective Area Fraction (CAF, Fig. 5 a),
270 defined as the ratio of area with $Z_H > 40$ dBZ (at 2 km a.g.l.) to total storm area. On average BoXPol observations show a bit
271 higher CAF compared to the simulations. The evolution is always similar in terms of an initial increase and intensification in
272 the second part of the observation period, where the experiment with maritime aerosols and low INP (Mar-lowIn) is closest to
273 observations. All simulations show Z_H and Z_{DR} patterns comparable to BoXPol observations, however, the experiment with
274 continental aerosol and default INP (Con-defIN, Fig. 5c) shows weaker Z_H , while Mar-lowIN (Fig. 5d) shows a bit higher Z_H
275 values compared to BoXPol (see Fig 5a). CN concentrations are 100 cm^{-3} for maritime and 1700 cm^{-3} for continental aerosol.
276 Similarly, concentrations for dust, soot and organics are $162\text{E}3 \text{ m}^{-3}$, $15\text{E}6 \text{ m}^{-3}$ and $177\text{E}6 \text{ m}^{-3}$, respectively, for default INP. For
277 low/high INP, the concentration of soot and organics are decreased/increased by one order of magnitude. The experiment with
278 continental aerosol and high INP concentration (Con-highIN, not shown) generates similar polarimetric moments like Con-
279 lowIN. All experiments show vertically extensive columns of (slightly) enhanced Z_{DR} , collocated with intense simulated
280 updrafts reaching up to 13 to 14 km height. Indeed, those Z_{DR} -columns emerged recently as proxies for updraft strength and
281 ensuing precipitation enhancement (Weissmann et al., 2014; Simmer et al., 2014; Kumjian et al., 2014), and research on their
282 exploitation for nowcasting and data assimilation is ongoing. In Fig. 5c/d synthetic Z_{DR} -columns are vertically extensive, while
283 Z_{DR} values within the column stay below 0.3 dB. BoXPol observations show Z_{DR} -columns reaching up to 6 km height only
284 but with Z_{DR} values exceeding 1dB. While Z_{DR} values in the lower part of the columns are mostly generated by large raindrops,
285 freezing drops and wet hail determine Z_{DR} in the upper parts of the column (Kumjian et al., 2014; Snyder et al., 2015). The
286 diverging appearance of observed and synthetic Z_{DR} columns may point to a deficiency in the treatment of raindrops
287 undergoing freezing and motivates further research. Too rapid freezing of drops combined with graupel generated from the
288 frozen drops may generate enhanced but still low Z_{DR} up to high altitudes. Following Ilotoviz et al. (2018) such attributes of
289 Z_{DR} columns are highly determined by the vertical velocity, hail size, and aerosol concentration, e.g. higher CN concentrations
290 lead to higher columns with higher Z_{DR} values inside and also higher Z_H . In this case study and the specific time step shown,



291 Mar-lowIN (i.e. with lower CN concentration) shows a wider and a bit taller Z_{DR} column together with a more intense Z_H core
292 (compare Fig. 5c/d). Further explanations, however, require an improved representation of the Z_{DR} -columns in the model.

293 **4 Fusion of radar polarimetry and atmospheric models**

294 Probably the most important and central tool for connecting polarimetric observations with numerical atmospheric models are
295 observation operators, which generate virtual observations from the model state. The latter can be directly compared with the
296 real observations and signatures of microphysical processes including their temporal evolution. Thus, the accuracy of
297 precipitation and cloud parameterizations can be indirectly evaluated, and a data base established for model optimization. E.g.
298 missing polarimetric process fingerprints (e.g. Kumjian, 2012) in the virtual observations may hint at model deficiencies, and
299 model parameterizations can be adapted in order to increase the coherence between real and virtual observations. Moreover,
300 appropriate observation operators are mandatory for the direct assimilation of observations using ensemble methods.

301 However, bulk cloud microphysical parameterizations required for NWP models include assumptions on several critical
302 parameters and processes to make up for lacking constraints from the governing numerical model. For example, in most
303 operational bulk schemes the melting state as well as shape, microstructure, and orientation of the different hydrometeors are
304 not prognostic (or not even implicitly assumed). These assumptions need also to be taken into account in observation operators
305 in order to create meaningful virtual observations. An example are the inherently assumed particle size distributions and their
306 relations to the prognostic moments. Moreover, bulk cloud microphysical schemes may only insufficiently approximate the
307 natural variability and interaction between small sets of assumed hydrometeor classes and size distribution moments mainly
308 tuned to get e.g. the surface precipitation right. Therefore, these current approximations in both numerical models and
309 observation operators may translate into different sources of errors and biases of the simulated radar variables (e.g. Schinagl
310 et al., 2019). An example can be seen in Figure 7, which will be discussed in Sect. 4.2.1. Such problems challenge both model
311 evaluation and data assimilation. Central science questions are therefore the realism of the sensitivities of simulated radar
312 variables to parameters in the observation operators and the models, and the effective approaches to the evaluation and
313 improvement of moist processes parametrizations.

314 **4.1 Radar observation operators**

315 The PROM-project *Operation Hydrometeors* extends the up to now non-polarimetric radar observation operator
316 EMVORADO (Zeng et al., 2016; Blahak and de Lozar, 2020; Blahak, 2016) to polarimetry (Mendrok et al., 2021) called Pol-
317 EMVORADO in the following. EMVORADO has been designed to efficiently simulate volume scan measurements of entire
318 radar networks from the prognostic model state of an NWP model. PPI volume scans can be simulated for many radar stations
319 simultaneously for direct comparisons with the radar observations. EMVORADO is part of both the COSMO and ICON NWP
320 model's executable and access model state variables in memory. The code is MPI- and OpenMP-parallelized and thus fully
321 exploits the computational power of modern HPCs and avoids storing and re-reading extensive model state data to/from hard



322 drives. This enables large-scale real-time applications such as operational data assimilation and extensive NWP model
323 verifications using whole radar networks at high temporal resolution. Its modular nature allows for relatively easy interface
324 development to other NWP models. An offline framework is also available, which accesses model states of one model time
325 step from hard disk. EMVORADO includes detailed modular schemes to simulate beam bending, beam broadening and
326 melting effects, and allows users to choose for each process between computationally cheap and physically accurate options.
327 The operator has been used for the assimilation of radar reflectivity with positive impact on precipitation forecasts (Bick et al.,
328 2016; Zeng et al., 2018, 2019, 2020). Currently, DWD uses EMVORADO to assimilate 3D volumetric reflectivity and radial
329 wind observations of its C-Band radar network. Key for this application is also the extensive use of precomputed lookup tables
330 which relate Mie-reflectivity to hydrometeors and temperature. The effects of neglecting reflectivity weighting, beam
331 broadening and fall speed on data assimilation have been investigated in a joint effort together with the PROM-project
332 **Representing model error and observation Error uncertainty for Data assimilation of POLarimetric radar measurements**
333 (**REDPOL**) (Zeng et al., 2021).

334 Pol-EMVORADO inherits all features of EMVORADO and expands them to polarimetric observables. This includes e.g. the
335 different beam bending, broadening and smoothing schemes, the effective medium approximations allowing 1- and 2-layered
336 hydrometeors with different water-ice-air mixing schemes and melting topologies, and the lookup table approach for an
337 efficient access to polarimetric observables such as Z_{DR} , LDR , ρ_{HV} , and K_{DP} . Optionally, attenuation effects and specific and
338 differential attenuation (A_H and A_{DP} , respectively) can be considered and further quantities derivable from the complex
339 scattering amplitudes can easily be added. Scattering properties of spheroidal particles derived by one-layered (Mishchenko,
340 2000) and two-layered T-Matrix approaches (Ryzhkov et al., 2011) are used instead of the “spherical” Mie-theory used in
341 EMVORADO. Assumptions on spheroid shape and orientation follow parametrizations introduced in Ryzhkov et al. (2011).
342 The lookup table approach has been revised to accommodate the additional parameters necessary to derive the full set of
343 polarimetric radar output.

344 Pol-EMVORADO is now incorporated into the official version of EMVORADO and can be run offline (i.e. stand-alone with
345 model fields from data files) and online (i.e. within a COSMO or ICON run). Designed as a PPI volume scan observation
346 operator for a radar network, its output can also be provided on NWP model grids. An example of a synthetic Z_{DR} from the
347 **REDPOL** project is given in Fig. 6 (see also Sec. 4.2.3).

348 Applying Pol-EMVORADO (or the related B-PRO, see Sect. 3.2) within PROM several issues became evident. Assuming
349 hydrometeors as homogeneous effective-medium particles (oblate spheroids) does not reproduce well the polarimetric
350 signatures of low density hydrometeors like dendrites or aggregates as typical in snow when keeping their microphysical
351 properties (e.g. aspect ratio, degree of orientation) within realistic - observed or model-predicted - ranges and consistent
352 between different radar frequencies. This deficiency has been demonstrated and explained from electromagnetic theory by
353 Schrom et al. (2018) and became also evident in the case study by Shrestha et al. (2021) and in Fig. 7, where Z_{DR} and K_{DP}
354 almost entirely lack the typical features in the snow-dominated layer between 2.5 and 5 km height. Orientation and shape of
355 frozen and melting hydrometeors are very variable both in nature and in the assumptions used in observation operators, which



356 translates in large uncertainties in polarimetric radar signatures (e.g., Matsui et al., 2019; Shrestha et al., 2021). To tackle these
357 challenges, Pol-EMVORADO will include in the future interfaces to several scattering databases or other scattering models in
358 order to enable more realistic cloud ice and aggregate snowflake scattering properties and allow for improvements or
359 extensions of the polarimetry-related microphysical assumptions (shape/habit/microstructure, orientation and their
360 distribution, e.g., Wolfensberger et al., 2018), particularly for (partly-)frozen hydrometeors. This will be taken up in PROM's
361 2nd phase guided with Lagrangian particle model information, as well as the test of Pol-EMVORADO in an operational data
362 assimilation environment.

363 4.2 Model evaluation and improvements using forward simulations and microphysical retrievals

364 4.2.1 Convection-resolving simulations with COSMO

365 In a joint effort, the PROM-projects *Operation Hydrometeors* and *ILACPR* evaluated simulated stratiform precipitation events
366 in radar observation space and developed a sophisticated polarimetry-based hydrometeor classification and quantification for
367 the evaluation of the representation of hydrometeors in numerical models. Based on a stratiform event monitored on 7 October
368 2014 with the Bonn polarimetric X-Band radar BoXPoI, Fig. 7 illustrates the potential of using polarimetric observations for
369 the evaluation and improvement of microphysical parametrisations. Fig. 7 a-f compare QVPs of measured and virtual Z_H , Z_{DR} ,
370 and K_{DP} with the Bonn Polarimetric Radar forward Operator B-PRO (Xie et al., 2021) to forecasts simulated with COSMO
371 version 5.1 using its 2-moment cloud microphysics scheme (itype_gscp=2683; Seifert and Beheng, 2016). Due to a small
372 spatial shift of the precipitation event in the simulations, the observations at 50.7305 N, 7.0717 E are compared with
373 simulations at a close-by grid-point at 51.1 N, 7.0717 E. As demonstrated in Shrestha et al. (2021) using a similar stratiform
374 precipitation event, COSMO tends to simulate considerable amounts of melting graupel partly reaching the surface, which
375 results within and below the melting layer (ML) to higher synthetic Z_{DR} than observed (compare Fig. 7c/d). Above the ML,
376 however, synthetic Z_{DR} already approaches 0 dB at around 6 km height, which indicates deficiencies in the ice-snow
377 partitioning in COSMO and the approximation of snow particles as soft spheroids in B-PRO leading in too low polarimetric
378 signals. While observed and simulated Z_H is comparable in terms of structure and magnitude, except a more pronounced
379 observed ML, larger differences exist with respect to K_{DP} above the ML (Fig. 7e/f). While observations show bands of
380 enhanced K_{DP} within the so-called dendritic growth layer centred around -12°C , the simulated K_{DP} is very weak indicating
381 lower crystal concentration and early aggregates compared to observations (e.g. Moisseev et al., 2015). Comparison of ice
382 water content (IWC) above the ML retrieved from measured K_{DP} and differential reflectivity in linear scale Z_{dr} , i.e. $IWC(K_{DP},$
383 $Z_{dr})$ following Ryzhkov et al. (2018), with the COSMO simulated IWC agrees well in terms of structure, but has lower
384 magnitudes (compare Fig. 7 g/h) in line with the lower simulated K_{DP} . Overall, Fig. 7 supports the hypothesis of a too strong
385 graupel production in simulations. *Operation Hydrometeors* also developed a robust radar-based hydrometeor classification
386 (HMC) and mixing ratio quantification algorithm following Grazioli et al. (2015) and Besic et al. (2016, 2018) for the
387 evaluation of the representation of hydrometeors in NWC models (standard output is the dominant hydrometeor type only).
388 The new method is relatively insensitive to uncertainties in the scattering properties of ice particles. Its application to the



389 BoXPol observations above does not indicate graupel below the ML (Fig. 8a), while COSMO simulates a pronounced, thick
390 graupel layer (Fig. 8b) including some melting graupel particles reaching the ground around 1:45 UTC. Applied to the virtual
391 observations, however, it does not reproduce a graupel layer of similar intensity (Fig. 8c), probably caused by a too strong Z_H
392 and temperature influence (compare with Fig. 7) relative to the polarimetric variables in the classification scheme which needs
393 further investigation. For the case study in Shrestha et al. (2021) the simulated graupel was even more pronounced and
394 sensitivity experiments were performed to guide model improvement. Increasing the minimum critical particle diameter D_{crit} ,
395 which is required for self-collection of ice particles (aggregation) increased/improved the ice-snow partitioning, and a lower
396 temperature threshold for snow and ice riming, T_{rime} , considerably reduced the graupel production.

397 Comparing state-of-the-art polarimetric retrievals of liquid water content (LWC), ice water content (IWC), particle number
398 concentration N_t and mean particle diameter D_m (e.g. Ryzhkov et al., 2018; Ryzhkov and Zrnica, 2019; Bukovčić et al., 2020;
399 Reimann et al., 2021; Trömel et al., 2019) with their simulated counterparts can also be used for evaluating NWP models and
400 for data assimilation (Carlin et al., 2016). E.g. Fig. 7g/h shows for the case study discussed earlier higher $IWC(K_{DP}, Z_{dr})$ than
401 simulated by COSMO. For more solid conclusions about possible model errors - and for the use of retrieved quantities for data
402 assimilation, the retrieval uncertainties must be estimated. The analysis of data collected in the ice regions of tropical
403 convective clouds indicates e.g., that $IWC(K_{DP}, Z_{dr})$ yields a root-mean-square error of of 0.49 gm^{-3} with the bias within 6%
404 (Nguyen et al., 2017; 2019).

405
406 The PROM-project *Polarimetric signatures of ice microphysical processes and their interpretation using in-situ*
407 *observations and cloud modeling POLICE* evaluates radar retrievals and models using in particular in-situ observations of
408 microphysical cloud parameters from the research aircrafts HALO (e.g. Wendisch et al., 2016; Voigt et al., 2017) and Falcon
409 (e.g. Voigt et al., 2010; Voigt et al., 2014; Flamant et al., 2017). Currently, ground-based polarimetric radar measurements and
410 aircraft in-situ data from the Olympic Mountain Experiment OLYMPEX (Houze et al., 2017; Heymsfield et al., 2018) are
411 exploited to investigate riming processes and to evaluate retrievals of ice water content (IWC), particle number concentration
412 N_t , and mean particle diameter D_m (e.g. Ryzhkov et al., 2018; Ryzhkov and Zrnica, 2019; Bukovčić et al., 2020). The
413 OLYMPEX mission took place on the Olympic Peninsula of Washington State (USA) from November 2015 through February
414 2016. The science aircraft University of North Dakota's (UND) Cessna Citation II equipped with an in-situ cloud payload
415 overpassed the National Science Foundation (NSF) Doppler On Wheels (DOW, mobile polarimetric X-band radar with about
416 60 km range and 74 m radial resolution), placed in the Chehalis Valley at Lake Quinault (47.48° N , 123.86° W , 64 m altitude)
417 performing RHI scans within an azimuthal sector of 22° . Measurements and microphysical retrievals of the DOW and the
418 Citation, respectively, are currently evaluated and will then be compared at matched space-time coordinates for several flight
419 transects.

420



421 4.2.2 Climate simulations with ICON-GCM

422 A major part of the uncertainties in representing clouds and precipitation in atmospheric models can be attributed to unresolved
423 variability that affects resolved variables via non-linear processes. Current climate model horizontal resolutions are of the
424 order of 100 km. But even for NWP models, which have resolutions between 10 km for global and 1 km for regional
425 simulations, most cloud processes remain unresolved. The project *Climate model Parameterizations informed by Radar*
426 (*PARA*) evaluates and improves the representation of cloud and precipitation processes in particular for climate models and
427 focuses on precipitation formation in ice clouds. Since most surface precipitation over continents and extra-tropical oceans
428 involve the ice phase (Mülmenstädt et al., 2015; Field and Heymsfield, 2015) its reliable representation is paramount and thus
429 the focus of *PARA*. Microphysical parameterizations typically consider only the mean cloud liquid or ice water content to
430 compute process rates, which causes biases in all non-linear processes including radiation (e.g., Cahalan 1994; Carlin et al.,
431 2002) and precipitation formation (e.g., Pincus and Klein, 2000). Realistic results thus require the tuning of process rates (e.g.,
432 Rotstajn 2000) or realistic estimates of subgrid-scale cloud variability and its inclusion in the process parameterizations. *PARA*
433 tries to exploit to this goal inherent model assumptions for treating fractional cloudiness. Since the early works of Sommeria
434 and Deardorff (1977), atmospheric models assume or predict some notion of subgrid-scale variability of relative humidity.
435 Some models do so by predicting cloud fraction (e.g., Tiedtke 1993), others use a diagnostic representation of the subgrid-
436 scale probability density function (PDF) of total water specific humidity, q_t (e.g., Sundqvist et al., 1989; Smith 1990; Le Treut
437 and Li, 1991; Rosch et al., 2015). Another option is to utilize a prognostic PDF of q_t by assuming a functional form and
438 predicting the shape parameters of the PDF (e.g., Tompkins 2002; Neggers 2009). The German climate and weather prediction
439 model ICON in its version dedicated to climate simulations (general circulation model version; ICON-GCM) inherits the
440 representation of physical processes from its predecessor ECHAM6 (Stevens et al., 2013) and uses the Sundqvist et al. (1989)
441 parameterization for a diagnostic PDF of the total-water specific humidity, q_t .

442 As a first step, *PARA* analysed the implied PDF of cloud ice using satellite observations from combined CloudSat-CALIPSO
443 radar-lidar satellite observations (DARDAR, Delanoë et al., 2014). Interestingly, a first direct comparison of IWC profiles
444 obtained from DARDAR with polarimetric retrievals based on the ground-based BoXPoL radar show an overall good
445 agreement, except for columns with an integrated ice water path IWP $> 1 \text{ kg m}^{-2}$. In these regions pronounced polarimetric
446 signatures result in high IWC at higher altitudes, which are neither reproduced by reflectivity-only retrievals nor by the
447 DARDAR retrievals. The statistics are currently evaluated on a larger data base, which is also used to investigate the impact
448 on the parameterizations in ICON-GCM. In the second step, a stochastic parameterisation approach is taken to allow for an
449 unbiased computation of cloud microphysical process rates on average. Based on the cumulative distribution function (CDF),
450 a random number generator draws from the CDF according to the simulated likelihood a plausible value of the specific ice
451 mass based on which the microphysical process is computed. This specifically considers the formation of solid precipitation
452 (snow) from ice clouds via aggregation and accretion processes (Lohmann and Roeckner, 1996; Stevens et al., 2013), and



453 subsequently the evaporation of precipitation below the clouds. The result of the revised aggregation parameterization is shown
454 in Fig. 9. The increased aggregation rate, which is a super-linear function of the specific cloud ice, q_i , leads to an average
455 decrease in q_i . The aggregation rate is directly linked to the accretion rate, which lowers the effect of q_i decrease. An
456 investigation of the influence of the revised aggregation parameterization on the different microphysical process rates - which
457 are related to the ice phase - is currently performed. A detailed evaluation of the new versus old parameterizations with ground-
458 based polarimetric radar is on its way, and will in particular focus on the time scales of evaporation of precipitation below the
459 cloud.

460 4.2.3 Data assimilation

461 Within an idealized framework, Jung et al. (2008, 2010) and Zhu et al. (2020) demonstrated benefits of assimilating simulated
462 polarimetric data for the estimation of microphysical state variables. Up to now, however, direct assimilation of real
463 polarimetric data poses great challenges due to the deficiencies of cloud and precipitation schemes in NWP models in
464 realistically representing and providing the necessary information (optimally the distribution of particle size, shape and
465 orientations in all model grid boxes) required by a polarimetric radar observation operator and therefore causing large
466 representation error (Janjic et al., 2018). Both, specification of model error to examine uncertainty in microphysics and
467 specification of observation error for polarimetric radar observations that include estimates of the representation error, are
468 investigated in the PROM-project *REDPOL*. For the assimilation of radar reflectivity with an ensemble Kalman filter, several
469 approaches for including model errors during data assimilation were explored, including 1) additive noise with samples
470 representing large-scale uncertainty (see Zeng et al., 2018), 2) combination of large scale and unresolved scale uncertainty
471 (Zeng et al., 2019), and finally 3) adding to these warm bubble triggering of convective storms in case they are missing in the
472 one hour forecast but present in corresponding observations (Zeng et al., 2020). Applying Pol-EMVORADO to the analysis
473 obtained by assimilating radar reflectivity (German C-Band network), Fig. 6 illustrates the resulting differences of these three
474 techniques in Z_{DR} -space. Obviously, synthetic Z_{DR} values depend on the strategy used to specify the model error, putting
475 another weight to the argument that assimilation of radar reflectivity alone is not sufficient to constrain the estimation of
476 microphysical state variables and that polarimetric information is required in addition. First results in this direction were
477 reported by Putnam et al. (2019), who assimilated Z_{DR} below the melting layer but reported problems in assimilation of K_{DP}
478 data.

479 5 Summary and Perspectives

480 The Priority Programme *Polarimetric Radar Observations meet Atmospheric Modelling (PROM)* (SPP 2115,
481 <https://www2.meteo.uni-bonn.de/spp2115/>) was established in April 2017 by the Senate of the Deutsche
482 Forschungsgemeinschaft (DFG, German Research Foundation) and is designed to run for six years. PROM is a coordinated
483 effort to foster partnerships between cloud modelers and radar meteorologists and thus to accelerate the exploitation of



484 polarimetric weather radars to improve the representation of cloud and precipitation processes in numerical models. The first
485 funding phase engaged in an as complete as possible exploitation and understanding of nation-wide polarimetric measurements
486 complemented by state-of-the measurement devices and techniques available at supersites. Bulk polarimetric measurements
487 available over Germany are complemented with multi-frequency observations and spectral polarimetry for detailed studies of
488 ice and cloud microphysics. Thus, for the first time, modellers hold three-dimensional microphysics-related observational data
489 in their hands to improve parameterisations. Key tools for the fusion of radar polarimetry and atmospheric modelling, e.g. the
490 Monte-Carlo Lagrangian particle model McSnow and the polarimetric observation operator Pol-EMVORADO have been
491 developed. PROM started with detailed investigations of the representation of cloud and precipitation processes in the COSMO
492 and ICON atmospheric models exploiting the polarimetric B-PRO and EMVORADO observation operators. First
493 improvements of the 2-moment cloud- and precipitation microphysics scheme are made and more are expected in phase 2.
494 Also intercomparisons of microphysic schemes in radar space have been performed. Phase 1 further developed microphysical
495 retrievals, determined their uncertainties and started their exploitation for model evaluation and radar-informed
496 parameterizations. Developed prerequisites pave the way to finally exploit polarimetry for indirect and direct data assimilation
497 in the upcoming second funding phase.

498 Some tools developed in Phase 1, however, still require refinement in Phase 2. The T-matrix calculations for
499 electromagnetic scattering by spheroidal particles represent only a crude approximation to frozen and mixed-phase
500 hydrometeors, especially for pristine ice particles and aggregate snowflakes at cloud radar wavelengths. It is not possible to
501 reproduce observed polarimetric signatures of snow with the T-Matrix approach (i.e. homogeneous ice-air spheroids) and
502 realistic microphysics (shape, orientation). Refinements include interfacing to a new discrete dipole approximation (DDA)-
503 based scattering data base for realistic ice and snow particles for all relevant weather radar wavelengths and improvements of
504 the melting scheme of graupel and hail.

505 Based on the made progress the fusion of radar polarimetry and atmospheric modelling can be approached even more
506 aggressively in Phase 2. While objective 1 received most attention in Phase 1, more projects will exploit now the observational
507 insights and tools developed to finally improve parameterizations and assimilate polarimetric information, i.e. more emphasis
508 will be put on Objectives 2 and 4 in Phase 2. Direct assimilation of polarimetric variables remains challenging, because NWP
509 models need to realistically represent and provide the necessary information required by a polarimetric radar observation
510 operator; ideally the distribution of particle size, shape and orientation would be required in all model grid boxes. Indirect
511 assimilation of polarimetric information (e.g. microphysical retrievals, and process signatures), however, is less demanding to
512 the model and should be pursued in parallel. Modern Bayesian data assimilation techniques are sensitive to both model- and
513 forward operator biases, so that further work on these issues is of great importance for a successful data assimilation.

514

515 **Data availability**



516 The data presented in this paper are available through the authors upon request. Polarimetric radar data from the operational
517 C-band radar network is also available from the German Weather Service (DWD). Specific campaign data will be published
518 in addition.

519

520 **Author contributions**

521 Silke Trömel had the initial idea and mainly organized and structured the joint publication. Silke Trömel, Johannes Quaas, and
522 Clemens Simmer formed the editorial team consolidating the text. All authors contributed to specific sections of the paper and
523 commented on the paper.

524

525 **Competing interests**

526 Johannes Quaas is editor of ACP. The authors declare to have no additional conflict of interest.

527

528 **Special issue statement**

529 This article is the overview article of the ACP/AMT/GMD inter-journal special issue “Fusion of radar polarimetry and
530 numerical atmospheric modelling towards an improved understanding of cloud and precipitation processes”. It is not associated
531 with a conference.

532

533 **Acknowledgments**

534 We gratefully acknowledge the funding of the German Research Foundation (DFG) to initialize the special priority program
535 on the Fusion of Radar Polarimetry and Atmospheric Modelling (SPP-2115, PROM). The work of contributing authors was
536 carried out in the framework of the projects Operation Hydrometeors (Grants TR 1023/16-1 and BL 945/2-1), ILACPR (Grant
537 SH 1326/1-1), POLICE (Grants TR 1023/13-1 and VO 1504/5-1), PARA (Grants QU 311/21-1 and TR 1023/15-1),
538 HydroColumn (FR 4119/1-1), REDPOL (Grant JA 1077/5-1), and PICNICC (Grants KA 4162/2-1 and SE 2464/1-1).

539

540 **References**

541 Alfieria, L., Thielen, J., and Pappenberger, J.: Ensemble hydro-meteorological simulation for flash flood early detection in
542 southern Switzerland, *J. Hydrol.*, 424, 143-153, doi:10.1016/j.jhydrol.2011.12.038, 2012.

543 Bauer, P., Thorpe, A., and Brunet, G.: The quiet revolution of numerical weather prediction, *Nature* 525, 47–55,
544 doi:10.1038/nature14956, 2015.

545 Besic, N., Gehring, J., Praz, C., Figueras i Ventura, J., Grazioli, J., Gabella, M., Germann, U., and Berne, A.: Unraveling
546 hydrometeor mixtures in polarimetric radar measurements, *Atmos. Meas. Tech.*, 11, 4847–4866, doi:10.5194/amt-11-4847-
547 2018, 2018.



- 548 Besic, N., Figueras i Ventura, J., Grazioli, J., Gabella, M., Germann, U., and Berne, A.: Hydrometeor classification through
549 statistical clustering of polarimetric radar measurements: A semisupervised approach. *Atmospheric Measurement Techniques*,
550 9(9), pp.4425-4445, 2016
- 551
- 552 Bick, T., Simmer, C., Trömel, S., Wapler, K., Stephan, K., Blahak, U., Zeng, Y., and Potthast, R.: Assimilation of 3D-radar
553 Reflectivities with an Ensemble Kalman Filter on the Convective Scale, *Quart. J. Roy. Meteor. Soc.*, 142, 1490–1504, 2016.
- 554
- 555 Blahak, U.: RADAR_MIE_LM and RADAR_MIELIB - Calculation of Radar Reflectivity from Model Output, COSMO
556 Technical Report No. 28, Consortium for Small Scale Modeling (COSMO), available online [http://www.cosmo-](http://www.cosmo-model.org/content/model/documentation/techReports/docs/techReport28.pdf)
557 [model.org/content/model/documentation/techReports/docs/techReport28.pdf](http://www.cosmo-model.org/content/model/documentation/techReports/docs/techReport28.pdf), 2016.
- 558
- 559 Blahak, U. and De Lozar, A.: EMVORADO - Efficient Modular VOLUME scan RADAR Operator. A User's Guide, Deutscher
560 Wetterdienst, available online http://www.cosmo-model.org/content/model/documentation/core/emvorado_userguide.pdf,
561 2020.
- 562
- 563 Brdar, S. and Seifert, A.: McSnow: A Monte-Carlo Particle Model for Riming and Aggregation of Ice Particles in a
564 Multidimensional Microphysical Phase Space, *J. Adv. Model. Earth Syst.*, 10(1), 187–206, doi:10.1002/2017MS001167, 2018.
- 565
- 566 Boucher, O., et al.: Clouds and aerosols, in *Climate Change 2013: The Physical Science Basis. Contribution of Working Group*
567 *I to the Fifth Assessment Report of the Intergovernmental Panel on Climate Change*, edited by T. Stocker, et al., pp. 571–658,
568 Cambridge University Press, Cambridge, United Kingdom and New York, NY, USA, 2013.
- 569
- 570 Bukovčić, P., Ryzhkov, A., and Zrnić, D.: Polarimetric Relations for Snow Estimation—Radar Verification, *Journal of Applied*
571 *Meteorology and Climatology*, 59(5), 991-1009, doi:10.1175/JAMC-D-19-0140.1, 2020
- 572
- 573 Bühl, J., Seifert, P., Wandinger, U., Baars, H., Kanitz, T., Schmidt, J., Myagkov, A., Engelmann, R., Skupin, A., Heese, B.,
574 Klepel, A., Althausen, D., and Ansmann, A.: LACROS: The Leipzig Aerosol and Cloud Remote Observations System, in:
575 *SPIE Remote Sensing*, edited by Comeron, A., Kassianov, E. I., Schäfer, K., Stein, K., and Gonglewski, J. D., p. 889002,
576 Dresden, Germany, doi:10.1117/12.2030911, 2013.
- 577
- 578 Cahalan, R. F.: Bounded cascade clouds: albedo and effective thickness, *Nonlinear Proc. In Geophysics.*, 1, 156-167, 1994.
- 579
- 580 Carlin, B., et al.: High-cloud horizontal inhomogeneity and solar albedo bias, *J. Climate*, 15, 2321 – 2339, 2002.



- 581
- 582 Carlin, J. T., Ryzhkov, A. V., Snyder, J. C., and Khain, A.: Hydrometeor Mixing Ratio Retrievals for Storm-Scale Radar Data
583 Assimilation: Utility of Current Relations and Potential Benefits of Polarimetry, *Monthly Weather Review* 144(8), 2981-3001,
584 doi:10.1175/MWR-D-15-461 0423.1., 2016.
- 585
- 586 Costa-Surós, M., Sourdeval, O., Acquistapace, C., Baars, H., Carbajal Henken, C., Genz, C., Hesemann, J., Jimenez, C., König,
587 M., Kretzschmar, J., Madenach, N., Meyer, C. I., Schrödner, R., Seifert, P., Senf, F., Brueck, M., Cioni, G., Engels, J. F., Fieg,
588 K., Gorges, K., Heinze, R., Siligam, P. K., Burkhardt, U., Crewell, S., Hoose, C., Seifert, A., Tegen, I., and Quaas, J.: Detection
589 and attribution of aerosol–cloud interactions in large-domain large-eddy simulations with the ICOSahedral Non-hydrostatic
590 model, *Atmos. Chem. Phys.*, 20, 5657–5678, doi:10.5194/acp-20-5657-2020, 2020.
- 591
- 592 Delanoë, J., Heymsfield, A. J., Protat, A., Bansemer, A., and Hogan, R. J.: Normalized particle size distribution for remote
593 sensing application, *J. Geophys. Res. Atmos.*, 119, 4204-4227, doi:10.1002/2013JD020700, 2014.
- 594
- 595 Diederich, M., Ryzhkov, A., Simmer, C., Zhang, P., and Trömel, S.: Use of specific attenuation for rainfall measurement at
596 X-band radar wavelengths - Part 1: Radar calibration and partial beam blockage estimation, *Journal of Hydrometeorology*, 16,
597 2, 487-502, doi: 10.1175/JHM-D-14-0066.1, 2015a.
- 598
- 599 Diederich, M., Ryzhkov, A., Simmer, C., Zhang, P., and Trömel, S.: Use of specific attenuation for rainfall measurement at
600 X-band radar wavelengths - Part 2: Rainfall estimates and comparison with rain gauges, *Journal of Hydrometeorology*, 16, 2,
601 503-516, doi: 10.1175/JHM-D-14-0067.1, 2015b.
- 602
- 603 Dipankar, A., Stevens, B., Heinze, R., Moseley, C., Zängl, G., Giorgetta, M., and Brdar, S.: Large eddy simulations using the
604 general circulation model ICON, *J. Adv. Model. Earth Sy.*, 7, 963–986, doi.org/10.1002/2015MS000431, 2015.
- 605
- 606 Field, P. R. and Heymsfield, A. J.: Importance of snow to global precipitation, *Geophys. Res. Lett.*, 42, 9512–9520,
607 doi:10.1002/2015GL065497, 2015.
- 608
- 609 Gasper, F., Görden, K., Shrestha, P., Sulis, M., Rihani, J., Geimer, M., and Kollet, S.: Implementation and scaling of the fully
610 coupled Terrestrial Systems Modeling Platform (TerrSysMP v1. 0) in a massively parallel supercomputing environment—a
611 case study on JUQUEEN (IBM Blue Gene/Q). *Geoscientific model development*, 7(5), 2531-2543, 2014.
- 612
- 613 Grazioli, J., Tuia, D., and Berne, A.: Hydrometeor classification from polarimetric radar measurements: a clustering approach.
614 *Atmospheric Measurement Techniques*, 8(1), pp.149-170, 2015.



- 615
- 616 Flamant, C., Knippertz, P., Fink, A.H., Akpo, A., Brooks, B., Chiu, C.J., Coe, H., Danuor, S., Evans, M., Jegede, O., Kalthoff,
617 N., Konaré, A., Lioussé, C., Lohou, F., Mari, C., Schlager, H., Schwarzenboeck, A., Adler, B., Amekudzi, L., Aryee, J.,
618 Ayoola, M., Batenburg, A.M., Bessardon, G., Borrmann, S., Brito, J., Bower, K., Burnet, F., Catoire, V., Colomb, A., Denjean,
619 C., Fosu-Amankwah, K., Hill, P.G., Lee, J., Lathon, M., Maranan, M., Marsham, J., Meynadier, R., Ngamini, J., Rosenberg,
620 P., Sauer, D., Smith, V., Stratmann, G., Taylor, J.W., Voigt, C., and Yoboué, V.: The Dynamics–Aerosol–Chemistry–Cloud
621 Interactions in West Africa Field Campaign: Overview and Research Highlights, *Bull. Amer. Meteor. Soc.*, 99, 83–104,
622 <https://doi.org/10.1175/BAMS-D-16-0256.1>, 2018
- 623
- 624 Hashino, T., and Tripoli, G. J.: The Spectral Ice Habit Prediction System (SHIPS). Part I: Model Description and Simulation
625 of the Vapor Deposition Process, *Journal of the Atmospheric Sciences*, 64(7), 2210–2237, doi:10.1175/JAS3963.1, 2007.
- 626
- 627 Heinze, R., Dipankar, A., Henken, C. C., Moseley, C., Sourdeval, O., Trömel, S., Xie, X., Adamidis, P., Ament, F., Baars, H.
628 Barthlott, C., Behrendt, A., Blahak, U., Bley, S., Brdar, S., Brueck, M., Crewell, S., Deneke, H., Girolamo, P. D., Evaristo,
629 R., Fischer, J., Frank, C., Friederichs, P., Göcke, T., Gorges, K., Hande, L., Hanke, M., Hansen, A., Hege, H.-C., Hoose, C.,
630 Jahns, T., Kalthoff, N., Klocke, D., Kneifel, S., Knippertz, P., Kuhn, A., Laar, T., Macke, A., Maurer, V., Mayer, B., Meyer,
631 C. I., Muppa, S. K., Neggers, R. A. J., Orlandi, E., Pantillon, F., Pospichal, B., Röber, N., Scheck, L., Seifert, A., Seifert, P.,
632 Senf, F., Siligam, P., Simmer, C., Steinke, S., Stevens, B., Wapler, K., Weniger, M., Wulfmeyer, V., Zängl, G., Zhang, D.,
633 and Quaas, J.: Large-eddy simulations over Germany using ICON: A comprehensive evaluation, *Quart. J. Roy. Meteorol. Soc.*,
634 143, 69–100, doi:10.1002/qj.2947, 2017.
- 635
- 636 Heymsfield, A., Bansemmer, A., Wood, N. B., Liu, G., Tanelli, S., Sy, O. O., Poellot, M., and Liu, C.: Toward Improving Ice
637 Water Content and Snow-Rate Retrievals from Radars. Part II: Results from Three Wavelength Radar–Collocated In Situ
638 Measurements and CloudSat–GPM–TRMM Radar Data, *Journal of Applied Meteorology and Climatology*, 57(2), 365–389.
639 Retrieved Apr 6, 2021, from <https://journals.ametsoc.org/view/journals/apme/57/2/jamc-d-17-0164.1.xml>, 2018.
- 640
- 641 Iltoviz, E., Khain, A., Ryzhkov, A. V., and Snyder, J. C.: Relation between Aerosols, Hail Microphysics, and ZDR Columns,
642 *J. Atmos. Sci.*, 75, 1755–1781, doi:10.1175/JAS-D-17-0127.1, 2018.
- 643
- 644 Janjic, T., Bormann, N., Bocquet, M., Carton, J. A., Cohn, S. E., Dance, S. L., Losa, S. N., Nichols, N. K., Potthast, R., Waller,
645 J. A., and Weston, P.: On the representation error in data assimilation, *Q. J. R. Meteorol. Soc.*, 144:713, 1257–1278, 2018.
- 646



- 647 Jung, Y., Xue, M., Zhang, G., and Straka, J.: Assimilation of simulated polarimetric radar data for a convective storm using
648 ensemble Kalman filter. Part II: Impact of polarimetric data on storm analysis, *Mon. Wea. Rev.*, 136, 2246–2260,
649 [doi:10.1175/2007MWR2288.1](https://doi.org/10.1175/2007MWR2288.1), 2008.
- 650
- 651 Jung, Y., Xue, M., and Zhang, G.: Simultaneous Estimation of Microphysical Parameters and the Atmospheric State Using
652 Simulated Polarimetric Radar Data and an Ensemble Kalman Filter in the Presence of an Observation Operator Error, *Mon.*
653 *Wea. Rev.*, 138, 539–562, [doi:10.1175/2009MWR2748.1](https://doi.org/10.1175/2009MWR2748.1), 2010.
- 654
- 655 Khain, A., Rosenfeld, D., and Pokrovsky, A.: Aerosol impact on the dynamics and microphysics of convective clouds, *Q. J.*
656 *R. Meteorol. Soc.*, 131, 2639–2663, [doi:10.1256/qj.04.62](https://doi.org/10.1256/qj.04.62), 2005.
- 657
- 658 Khain, A. P., Beheng, K. D., Heymsfield, A., Korolev, A., Krichak, S. O., Levin, Z., Pinsky, M., Phillips, V., Prabhakaran, T.,
659 Teller, A., et al.: Representation of microphysical processes in cloud-resolving models: Spectral (bin) microphysics versus
660 bulk parameterization, *Rev. Geophys.*, 53, 247–322, [doi:10.1002/2014RG000468](https://doi.org/10.1002/2014RG000468), 2015.
- 661
- 662 Kleine, J., Voigt, C., Sauer, D., Schlager, H., Scheibe, M., Kaufmann, S., Jurkat-Witschas, T., Kärcher, B., and Anderson B.:
663 In situ observations of ice particle losses in a young persistent contrail, *Geophys. Res. Lett.*, [doi:10.1029/2018GL079390](https://doi.org/10.1029/2018GL079390), 2018.
- 664
- 665 Kumjian, M. R.: The impact of precipitation physical processes on the polarimetric radar variables, Dissertation, University
666 of Oklahoma, Norman Campus, <https://hdl.handle.net/11244/319188>, 2012
- 667
- 668 Kumjian, M. R., Khain, A. P., Benmoshe, N., Ilotoviz, E., Ryzhkov, A. V., and Phillips, V. T. J.: The anatomy and physics of
669 Z_{DR} columns: Investigating a polarimetric radar signature with a spectral bin microphysical model, *Journal of Applied*
670 *Meteorology and Climatology*, 53, 1820-1843, 2014.
- 671
- 672 Le Treut, H. and Li, Z.-X.: Sensitivity of an atmospheric general circulation model to prescribed SST changes: Feedback
673 effects associated with the simulation of cloud optical properties, *Clim. Dyn.*, 5, 175–187, 1991.
- 674
- 675 Libbrecht, K. G.: The physics of snow crystals, *Rep. Prog. Phys.*, 68, 855–895, [doi:10.1088/0034-4885/68/4/R03](https://doi.org/10.1088/0034-4885/68/4/R03), 2005.
- 676
- 677 Lohmann U. und E. Roeckner, Design and performance of a new cloud microphysics scheme developed for the ECHAM
678 general circulation model. *Clim. Dyn.*, 12, 557-572, 1996.
- 679



- 680 Matsui, T., Dolan, B., Rutledge, S. A., Tao, W.-K., Iguchi, T., Barnum, J., and Lang, S. E.: POLARRIS: A POLARimetric
681 Radar Retrieval and Instrument Simulator, *Journal of Geophysical Research: Atmospheres*, 124, 4634–4657,
682 doi:10.1029/2018JD028317, 2019.
- 683
- 684 Mellado, J.P., Stevens, B., Schmidt, H., and Peters, N.: Buoyancy reversal in cloud-top mixing layers, *Q.J.R. Meteorol. Soc.*,
685 135: 963-978., doi:10.1002/qj.417, 2009.
- 686
- 687 Mendrok, J., Blahak, U., Snyder, J. C., and Carlin, J. T.: The polarimetric efficient modular volume scan radar forward operator
688 Pol-EMVORADO, *Geosci. Model Dev.*, 2021 (in preparation for this Special Issue).
- 689
- 690 Mishchenko, M. I.: Calculation of the amplitude matrix for a nonspherical particle in a fixed orientation, *Appl. Opt.* 39, 1026-
691 1031 (2000).
- 692
- 693 Moisseev, D. N., Lautaportti, S., Tyynela, J., and Lim, S.: Dualpolarization radar signatures in snowstorms: Role of snowflake
694 aggregation, *J. Geophys. Res. Atmos.*, 120, 12 644–12 655, doi:10.1002/2015JD023884, 2015.
- 695
- 696 Morrison, H. and Milbrandt, J. A.: Parameterization of Cloud Microphysics Based on the Prediction of Bulk Ice Particle
697 Properties. Part I: Scheme Description and Idealized Tests, *Journal of the Atmospheric Sciences*, 72(1), 287-311, 2015.
- 698
- 699 Mülmenstädt, J., Sourdeval, O., Delanoë, J., and Quaas, J.: Frequency of occurrence of rain from liquid-, mixed- and ice-phase
700 clouds derived from A-Train satellite retrievals, *Geophys. Res. Lett.*, 42, 6502-6509, doi:10.1002/2015GL064604, 2015.
- 701
- 702 Myagkov, A., Seifert, P., Bauer-Pfundstein, M., and Wandinger, U.: Cloud radar with hybrid mode towards estimation of
703 shape and orientation of ice crystals, *Atmos. Meas. Tech.*, 9, 469–489, doi:10.5194/amt-9-469-2016, 2016.
- 704
- 705 Neggers, R. A.: A dual mass flux framework for boundary layer convection. Part II: Clouds, *J. Atmos. Sci.*, 66, 1489–1506,
706 doi:10.1175/2008JAS2636.1, 2009.
- 707
- 708 Neto, J. D., Kneifel, S., Ori, D., Trömel, S., Handwerker, J., Bohn, B., Hermes, N., Mühlbauer, K., Lenefer, M., and Simmer,
709 C.: The TRIPLE-frequency and Polarimetric radar Experiment for improving process observation of winter precipitation. *Earth*
710 *Syst. Sci. Data*, 11, 845–863, doi: 10.5194/essd-11-845-2019, 2019.
- 711



- 712 Nguyen, C., Wolde, M., Baibakov, K., and Korolev, A.: Detection and estimation of high ice water content using X- and W-
713 band dual-polarization airborne radar data, 38th Conf. on Radar Meteorology, Chicago, IL, Amer. Meteor. Soc., 89,
714 <https://ams.confex.com/ams/38RADAR/webprogram/Paper321101.html>, 2017.
- 715
- 716 Nguyen, C. M., Wolde, M., and Korolev, A.: Determination of ice water content (IWC) in tropical convective clouds from X-
717 band dual-polarization airborne radar. Atmos. Meas. Tech., 12, 5897–5911, [doi: 10.5194/amt-12-5897-2019](https://doi.org/10.5194/amt-12-5897-2019), 2019.
- 718
- 719 Ori, D., V. Schemann, M. Karrer, J. Dias Neto, L. von Terzi, A. Seifert, and S. Kneifel: Evaluation of ice particle growth in
720 ICON using statistics of multi-frequency Doppler cloud radar observations, Q. J. Roy. Meteor. Soc., 146: 3830– 3849.
721 <https://doi.org/10.1002/qj.3875>, 2020
- 722
- 723 Pincus, R. and Klein, S.: Unresolved spatial variability and microphysical process rates in large-scale models, J. Geophys.
724 Res., 105, 27059 - 27065, 2000.
- 725
- 726 Putnam, B., Xue, M., Jung, Y., Snook, N., and Zhang, G.: Ensemble Kalman Filter Assimilation of Polarimetric Radar
727 Observations for the 20 May 2013 Oklahoma Tornadoic Supercell Case, Mon. Wea. Rev., 147, 2511–2533, [doi:10.1175/MWR-](https://doi.org/10.1175/MWR-D-18-0251.1)
728 [D-18-0251.1](https://doi.org/10.1175/MWR-D-18-0251.1), 2019.
- 729
- 730 Reimann, L., Simmer, C., and Trömel, S.: Dual-polarimetric radar estimators of liquid water content over Germany. Accepted
731 for Meteorol. Z. (Contrib. Atm. Sci.), [doi:10.1127/metz/2021/1072](https://doi.org/10.1127/metz/2021/1072), 2021.
- 732
- 733 Rosch, J., et al.: Analysis of diagnostic climate model cloud parameterisations using large-eddy simulations, Q. J. R. Meteorol.
734 Soc., 141, 2199-2205, [doi:10.1002/qj.2515](https://doi.org/10.1002/qj.2515), 2015.
- 735
- 736 Rotstayn, L. D.: On the tuning of autoconversion parameterizations in climate models, J. Geophys. Res., 105, 15,495–15,507,
737 2000.
- 738
- 739 Ryzhkov, A. V., Zrnich, D. S., and Gordon, B. A.: Polarimetric Method for Ice Water Content Determination. Journal of Applied
740 Meteorology 37, 125-134, 1998.
- 741
- 742 Ryzhkov, A., Pinsky, M., Pokrovsky, A., and Khain, A.: Polarimetric Radar Observation Operator for a Cloud Model with
743 Spectral Microphysics, J. Appl. Meteor. Climat., 50, 873-894, 2011.



- 744
- 745 Ryzhkov, A., Zhang, P., Reeves, H., Kumjian, M., Tschallener, T., Trömel, S., and Simmer, C.: Quasi-vertical profiles – a
746 new way to look at polarimetric radar data, *J. Atmos. Oceanic Technol.*, 33, 551-562, [doi: 10.1175/JTECH-D-15-0020.1](https://doi.org/10.1175/JTECH-D-15-0020.1), 2016.
- 747
- 748 Ryzhkov, A., Bukovcic, P., Murphy, A., Zhang, P., and McFarquhar, G.: Ice Microphysical Retrievals Using Polarimetric
749 Radar Data. In Proceedings of the 10th European Conference on Radar in Meteorology and Hydrology, Ede, The Netherlands,
750 1–6 July 2018.
- 751
- 752 Ryzhkov, A. and Zrnich, D.: Radar Polarimetry for Weather Observations, Springer Atmospheric Sciences, 486 pp., 2019.
- 753
- 754 Schinagl, K., Friederichs, P., Trömel, S., and Simmer, C.: Gamma Drop Size Distribution Assumptions in Bulk Model
755 Parameterizations and Radar Polarimetry and Their Impact on Polarimetric Radar Moments, *J. Appl. Meteor. Climatol.*, 58,
756 467–478, [doi: 10.1175/JAMC-D-18-0178.1](https://doi.org/10.1175/JAMC-D-18-0178.1), 2019.
- 757
- 758 Schrom, R. S. and Kumjian, M. R.: Bulk-Density Representations of Branched Planar Ice Crystals: Errors in the Polarimetric
759 Radar Variables, *Journal of Applied Meteorology and Climatology*, 57(2), 333-346, 2018.
- 760
- 761 Seifert, A. and Beheng, K. D.: A two-moment cloud microphysics parameterization for mixed-phase clouds. Part 1: Model
762 description, *Meteorol. Atmos. Phys.*, 92, 45-66, DOI: 10.1007/s00703-005-0112-4, 2006.
- 763
- 764 Shrestha, P., Sulis, M., Masbou, M., Kollet, S. and Simmer, C: A scale-consistent Terrestrial System Modeling Platform based
on COSMO, CLM and ParFlow, *Mon. Wea. Rev.*, 142, 3466-3483, doi: 10.1175/MWR-D-14-00029.1, 2014
- 765
- 766 Shrestha, P.: Clouds and vegetation modulate shallow groundwater table depth. Accepted for publication in *Journal of
Hydrometeorology*, 2021
- 767
- 768 Shrestha, P., Mendrok, J., Pejčic, V., Trömel, S., and Blahak, U.: The impact of uncertainties in model microphysics, retrievals
and forward operators on model evaluations in polarimetric radar space, *Atmos. Chem. Phys.*, 2021 (close to submission for
769 this Special Issue).
- 770
- 771 Simmel, M., Bühl, J., Ansmann, A., and Tegen, I.: Ice phase in altocumulus clouds over Leipzig: remote sensing observations
772 and detailed modeling. *Atmos. Chem. Phys.*, 15, 10453–10470, doi:10.5194/acp-15-10453-2015, 2015.
- 773
- 774 Simmer, C., Thiele-Eich, I., Masbou, M., Amelung, W., Crewell, S., Diekkruöger, B., Ewert, F., Hendricks Franssen, H.-J.,
775 Huisman, A. J., Kemna, A., Klitzsch, N., Kollet, S., Langensiepen, M., Löhnert, U., Rahman, M., Rascher, U., Schneider, K.,



- 776 Schween, J., Shao, Y., Shrestha, P., Stiebler, M., Sulis, M., Vanderborcht, J., Vereecken, H., van der Kruk, J., Zerenner, T.,
777 and Waldhoff, G.: Monitoring and Modeling the Terrestrial System from Pores to Catchments - the Transregional
778 Collaborative Research Center on Patterns in the Soil-Vegetation-Atmosphere System, *Bulletin of the American*
779 *Meteorological Society*, 96, 1765–1787. doi: <http://dx.doi.org/10.1175/BAMS-D-13-00134.1>, 2015.
- 780
- 781 Simmer, C., Adrian, G., Jones, S., Wirth, V., Goeber, M., Hohenegger, C., Janjic, T., Keller, J., Ohlwein, C., Seifert, A.,
782 Trömel, S., Ulbrich, T., Wapler, K., Weissmann, M., Keller, J., Masbou, M., Meilinger, S., Riss, N., Schomburg, A., Vormann,
783 A., and Weingaertner, C.: HErZ - The German Hans-Ertel Centre for Weather Research. *Bulletin of the American*
784 *Meteorological Society*, p.1057-1068, DOI: <http://dx.doi.org/10.1175/BAMS-D-13-00227.1>, 2014
- 785
- 786 Smith, R. N.: A scheme for predicting layer clouds and their water content in a general circulation model, *Q. J. R. Meteorol.*
787 *Soc.*, 116, 435–460, doi:10.1002/qj.49711649210, 1990.
- 788
- 789 Snyder, J.C., Ryzhkov, A.V., Kumjian, M.R., Khain, A.P., and Picca, J.C.: A ZDR column detection algorithm to examine
790 convective storm updrafts, *Weather and Forecasting*, 30, 1819-1844, 2015.
- 791
- 792 Sommeria, G. and Deardorff, J. W.: Subgrid-scale condensation models of non-precipitating clouds, *J. Atmos. Sci.*, 34, 344-
793 355, 1977.
- 794
- 795 Sourdeval, O., Gryspeerd, E., Krämer, M., Goren, T., Delanoë, J., Afchine, A., Hemmer, F., and Quaas, J.: Ice crystal number
796 concentration estimates from lidar–radar satellite remote sensing – Part 1: Method and evaluation, *Atmos. Chem. Phys.*, 18,
797 14327–14350, doi: [10.5194/acp-18-14327-2018](https://doi.org/10.5194/acp-18-14327-2018), 2018.
- 798
- 799 Stevens, B., Acquistapace, C., Hansen, A., Heinze, R., Klinger, C., Klocke, D., Schubotz, W., Windmiller, J., Adamidis, P.,
800 Arka, I., Barlakas, V., Biercamp, J., Brueck, M., Brune, S., Buehler, S., Burkhardt, U., Cioni, G., Costa-Surós, M., Crewell,
801 S., Crueger, T., Deneke, H., Friederichs, P., Carbajal Henken, C., Hohenegger, C., Jacob, M., Jakob, F., Kalthoff, N., Köhler,
802 M., Van Laar, T. W., Li, P., Löhnert, U., Macke, A., Madenach, N., Mayer, B., Nam, C., Naumann, A. K., Peters, K., Poll, S.,
803 Quaas, J., Röber, N., Rochetin, N., Rybka, H., Scheck, L., Schemann, V., Schnitt, S., Seifert, A., Senf, F., Shapkalijevski,
804 M., Simmer, C., Singh, S., Sourdeval, O., Spickermann, D., Strandgren, J., Tessiot, O., Vercauteren, N., Vial, J., Voigt, A.,
805 and Zängl, G.: Large-eddy and storm resolving models for climate prediction - the added value for clouds and precipitation, *J.*
806 *Meteorol. Soc. Japan*, 98, doi:10.2151/jmsj.2020-021, 2020.
- 807
- 808 Stevens, B., et al.: Atmospheric component of the MPI-M Earth System Model: ECHAM6, *J. Adv. Model. Earth Syst.* 5: 146–
809 172, doi: [10.1002/jame.20015](https://doi.org/10.1002/jame.20015), 2013.



- 810
811 Stevens, B. and Feingold, G.: Untangling Aerosol Effects on Clouds and Precipitation in a Buffered System, *Nature*, 461, 607-
812 613, 2009.
- 813
814 Sundqvist, H., et al., Condensation and cloud parameterization studies with a mesoscale numerical weather prediction model,
815 *Mon. Weather Rev.*, 117, 1641–1657, 1989.
- 816
817 Takahashi, T.: High ice crystal production in winter cumuli over the Japan Sea, *Geophysical research letters*, 20.6, 451-454,
818 1993.
- 819
820 Takahashi, T., Yoshihiro N., and Yuzuru K.: Possible high ice particle production during graupel–graupel collisions, *Journal*
821 *of the atmospheric sciences*, 52.24, 4523-4527, 1995.
- 822
823 Takahashi, T.: Influence of liquid water content and temperature on the form and growth of branched planar snow crystals in
824 a cloud. *Journal of the Atmospheric Sciences*, 71.11, 4127-4142, 2014.
- 825
826 Tiedtke, M.: Representation of clouds in large scale models, *Mon. Weather Rev.*, 121, 3040–3061, 1993.
- 827
828 Tompkins, A.: A prognostic parameterization for the subgrid-scale variability of water vapor and clouds in large-scale models
829 and its use to diagnose cloud cover, *J. Atmos. Sci.*, 59:1917- 1942, 2002.
- 830
831 Trömel, S., Quaas, J., Crewell, S., Bott, A., and Simmer, C.: Polarimetric Radar Observations Meet Atmospheric Modelling.
832 19th International Radar Symposium (IRS), Bonn, doi: 10.23919/IRS.2018.8448121, URL:
833 <http://ieeexplore.ieee.org/stamp/stamp.jsp?tp=&arnumber=8448121&isnumber=8447894>, 2018.
- 834
835 Trömel, S., Ryzhkov, A. V., Hickman, B., Mühlbauer, K., and Simmer, C.: Polarimetric Radar Variables in the Layers of
836 Melting and Dendritic Growth at X Band—Implications for a Nowcasting Strategy in Stratiform Rain, *J. Appl. Meteor.*
837 *Climatol.*, 58, 2497–2522, <https://doi.org/10.1175/JAMC-D-19-0056.1>, 2019.
- 838
839 Trömel, S., A. V. Ryzhkov, P. Zhang, and C. Simmer: The microphysical information of backscatter differential phase δ in the
840 melting layer. *Journal of Applied Meteorology and Climatology*, 53, 2344-2359, 2014.
- 841
842 Voigt, C., Schumann, U., Jurkat, T., Schäuble, D., Schlager, H., Petzold, A., Gayet, J.-F., Krämer, M., Schneider, J., Borrmann,
843 S., Schmale, J., Jessberger, P., Hamburger, T., Lichtenstern, M., Scheibe, M., Gourbeyre, C., Meyer, J., Kübbeler, M., Frey,



- 844 W., Kalesse, H., Butler, T., Lawrence, M. G., Holzäpfel, F., Arnold, F., Wendisch, M., Döpelheuer, A., Gottschaldt, K.,
845 Baumann, R., Zöger, M., Sölch, I., Rautenhaus, M., and Dörnbrack, A.: In-situ observations of young contrails – overview
846 and selected results from the CONCERT campaign, *Atmos. Chem. Phys.*, 10, 9039–9056, [https://doi.org/10.5194/acp-10-](https://doi.org/10.5194/acp-10-9039-2010)
847 9039-2010, 2010.
- 848
- 849 Voigt, C., Jeßberger, P., Jurkat, T., Kaufmann, S., Baumann, R., Schlager, H., Bobrowski, N., Guffirda, G., and Salerno, G.:
850 Evolution of CO₂, SO₂, HCl and HNO₃ in the volcanic plumes from Etna, *Geophys. Res. Lett.*, 41,
851 doi:10.1002/2013GL058974, 2014.
- 852
- 853 Voigt, C., Schumann, U., Minikin, A., Abdelmonem, A., Afchine, A., Borrmann, S., Boettcher, M., Buchholz, B., Bugliaro,
854 L., Costa, A., Curtius, J., Dollner, M., Dörnbrack, A., Dreiling, V., Ebert, V., Ehrlich, A., Fix, A., Forster, L., Frank, F.,
855 Fütterer, D., Giez, A., Graf, K., Groß, J., Groß, S., Heimerl, K., Heinold, B., Hüneke, T., Järvinen, E., Jurkat, T., Kaufmann,
856 S., Kenntner, M., Klingebiel, M., Klimach, T., Kohl, R., Krämer, M., Krisna, T. C., Luebke, A., Mayer, B., Mertes, S.,
857 Molleker, S., Petzold, A., Pfeilsticker, K., Port, M., Rapp, M., Reutter, P., Rolf, C., Rose, D., Sauer, D., Schäfler, A., Schläge,
858 R., Schnaiter, M., Schneider, J., Spelten, N., Spichtinger, P., Stock, P., Walser, A., Weigel, R., Weinzierl, B., Wendisch, M.,
859 Werner, F., Wernli, H., Wirth, M., Zahn, A., Ziereis, H., and Zöger, M.; ML-CIRRUS: The Airborne Experiment on Natural
860 Cirrus and Contrail Cirrus with the High-Altitude Long-Range Research Aircraft HALO, *Bulletin of the American*
861 *Meteorological Society*, 98(2), 271-288, doi:[bams-d-15-00213.1](https://doi.org/10.1175/BAMS-D-15-00213.1), 2017.
- 862 Voigt, C., Lelieveld, J., Schlager, H., Schneider, J., Sauer, D., Meerkötter, R., Pöhlker, M., Bugliaro, L., Curtius, J.,
863 Erbertseder, T., Hahn, V., Jöckel, P., Li, Q., Marsing, A., Mertens, M., Pöhlker, C., Pöschl, U., Pozzer, A., Tomsche, L., and
864 Schumann, U.: Aerosol and Cloud Changes during the Corona Lockdown in 2020 - First highlights from the BLUESKY
865 campaign; EGU21-13134, <https://meetingorganizer.copernicus.org/EGU21/session/40818>, 2021.
- 866 Weissmann, M., M. Göber, C. Hohenegger, T. Janjic, J. Keller, C. Ohlwein, A. Seifert, S. Trömel, T. Ulbrich, K. Wapler, C.
867 Bollmeyer, H. Deneke: The Hans-Ertel Centre for Weather Research – Research objectives and highlights from its first three
868 years. *Meteorol. Z.*, 23(3), 193 – 208, 2014.
- 869 Wendisch, M., Pöschl, U., Andreae, M. O., Machado, L. A. T., Albrecht, R., Schlager, H., Rosenfeld, D., Martin, S. T.,
870 Abdelmonem, A., Afchine, A., Araùjo, A. C., Artaxo, P., Aufmhoff, H., Barbosa, H. M. J., Borrmann, S., Braga, R., Buchholz,
871 B., Cecchini, M. A., Costa, A., Curtius, J., Dollner, M., Dorf, M., Dreiling, V., Ebert, V., Ehrlich, A., Ewald, F., Fisch, G.,
872 Fix, A., Frank, F., Fütterer, D., Heckl, C., Heidelberg, F., Hüneke, T., Jäkel, E., Järvinen, E., Jurkat, T., Kanter, S., Kästner,
873 U., Kenntner, M., Kesselmeier, J., Klimach, T., Knecht, M., Kohl, R., Kölling, T., Krämer, M., Krüger, M., Krisna, T. C.,
874 Lavric, J. V., Longo, K., Mahnke, C., Manzi, A. O., Mayer, B., Mertes, S., Minikin, A., Molleker, S., Münch, S., Nillius, B.,
875 Pfeilsticker, K., Pöhlker, C., Roiger, A., Rose, D., Rosenow, D., Sauer, D., Schnaiter, M., Schneider, J., Schulz, C., de Souza,



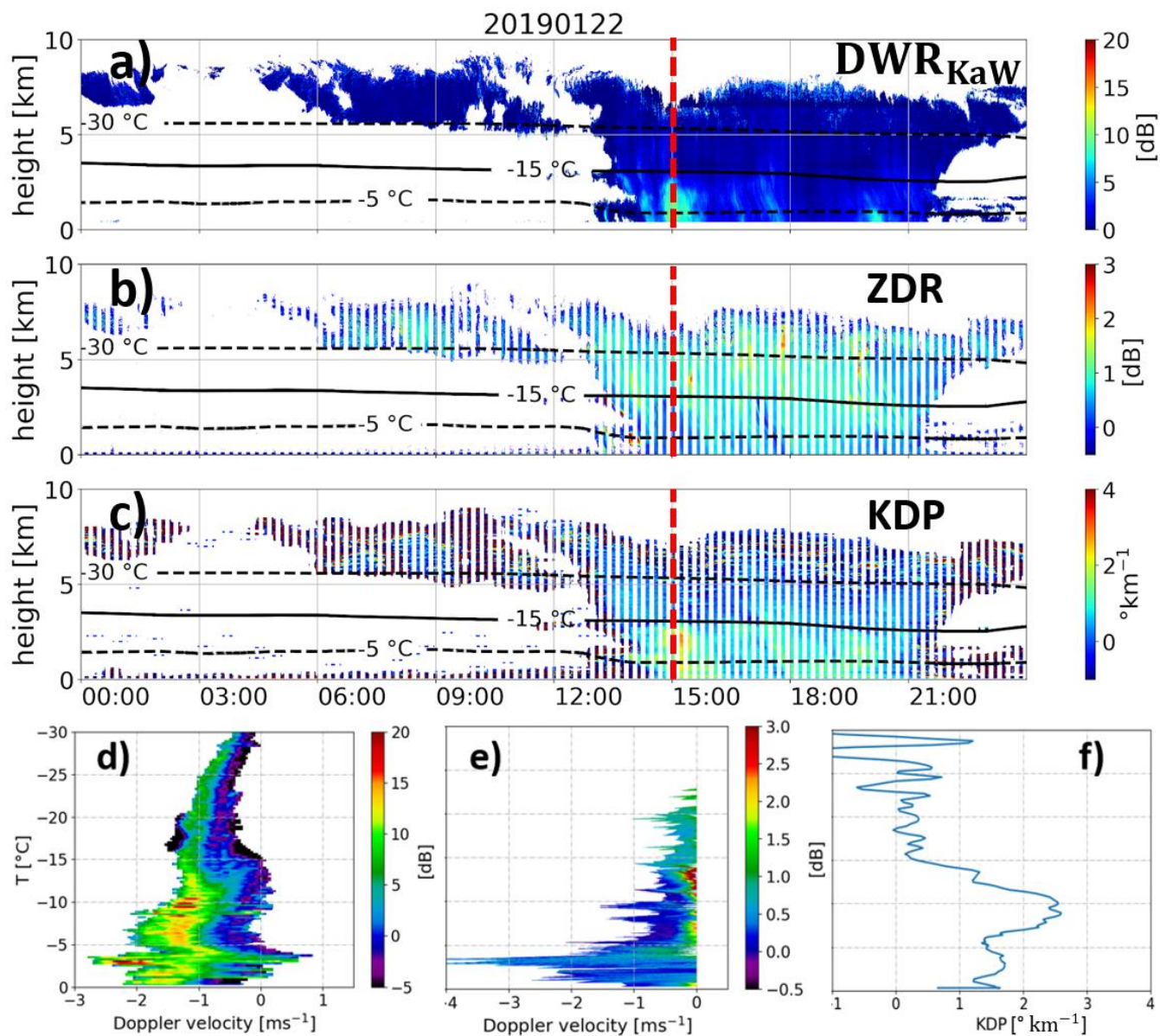
- 876 R. A. F., Spanu, A., Stock, P., Vila, D., Voigt, C., Walser, A., Walter, D., Weigel, R., Weinzierl, B., Werner, F., Yamasoe, M.
877 A., Ziereis, H., Zinner, T., and Zöger, M.: ACRIDICON–CHUVA Campaign: Studying Tropical Deep Convective Clouds and
878 Precipitation over Amazonia Using the New German Research Aircraft HALO, *Bulletin of the American Meteorological*
879 *Society*, 97(10), 1885–1908, doi:[bams-d-14-00255.1](https://doi.org/10.1175/BAMS-D-14-00255.1), 2016.
- 880 Wolfensberger, D. and Berne, A.: From model to radar variables: a new forward polarimetric radar operator for COSMO,
881 *Atmos. Meas. Tech.*, 11, 3883–3916, doi: 10.5194/amt-11-3883-2018, 2018.
- 882 Xie, X., Evaristo, R., Trömel, S., Saavedra, P., Simmer, C., and Ryzhkov, A.: Radar Observation of Evaporation and
883 Implications for Quantitative Precipitation and Cooling Rate Estimation, *J. Atmos. Oceanic Technol.* 33(8), 1779–1792,
884 [doi:10.1175/JTECH-D-15-0244.1](https://doi.org/10.1175/JTECH-D-15-0244.1), 2016.
- 885
- 886 Xie, X., Shrestha, P., Mendrok, J., Carlin, J., Trömel, S., and Blahak, U.: Bonn Polarimetric Radar forward Operator (B-PRO),
887 CRC/TR32 Database (TR32DB), doi:10.5880/TR32DB.41, 2021, (accessed 8 April 2021).
- 888
- 889 Zängl, G., et al.: The ICON (icosahedral non-hydrostatic) modelling framework of DWD and MPI-M: Description of the non-
890 hydrostatic dynamical core; *Quart. J. Roy. Meteorol. Soc.*, 141, 563–579, 2015.
- 891
- 892 Zeng, Y., Janjic, T., Lozar, A. de, Welzbacher, C. A., Blahak, U., and Seifert, A.: Assimilating radar radial wind and reflectivity
893 data in an idealized setup of the COSMO-KENDA system, *Atmospheric Research*, 249, 105282,
894 [doi:10.1016/j.atmosres.2020.105282](https://doi.org/10.1016/j.atmosres.2020.105282), 2021.
- 895
- 896 Zeng, Y., Janjic, T., Lozar, A. de, Rasp, S., Blahak, U., Seifert, A., and Craig, G. C.: Comparison of methods accounting for
897 subgrid-scale model error in convective-scale data assimilation, *Mon. Wea. Rev.*, 148, 2457–2477, 2020.
- 898
- 899 Zeng Y., Janjic, T., Sommer, M., Lozar, A. de, Blahak, U., and Seifert, A.: Representation of model error in convective-scale
900 data assimilation: additive noise based on model truncation error, *J. Advances in Modelling Earth Systems*, 11, 752–770, 2019.
- 901
- 902 Zeng, Y., Janjic, T., Lozar, A. de, Blahak, U., Reich, H., Keil, C., and Seifert, A.: Representation of model error in convective-
903 scale data assimilation: Additive noise, relaxation methods and combinations, *J. Advances in Modelling Earth Systems*, 10,
904 2889–2911, 2018.
- 905



906 Zeng, Y., Blahak, U., and Jerger, D.: An efficient modular volume-scanning radar forward operator for NWP models:
907 description and coupling to the COSMO model, Quarterly Journal of the Royal Meteorological Society, 142(701), 3234-3256,
908 2016

909
910 Zhu, K., Xue, M., Ouyang, K., and Jung, Y.: Assimilating polarimetric radar data with an ensemble Kalman filter: OSSEs with
911 a tornadic supercell storm simulated with a two-moment microphysics scheme, Q. J. R. Meteorol. Soc., 146: 1880– 1900,
912 [doi:10.1002/qj.3772](https://doi.org/10.1002/qj.3772), 2020.

913
914



915

916

Figure 1: Observations at JOYCE-CF shows a) DWR_{KaW}, b) ZDR (measured at a 30° elevation angle), c) KDP (also measured at 30° elevation angle) on 22.01.2019. Panels d)-f) show the observed DWR-spectrum, ZDR-spectrum and KDP-profile at 15:00 UTC (indicated by the red line in panels a)-c))

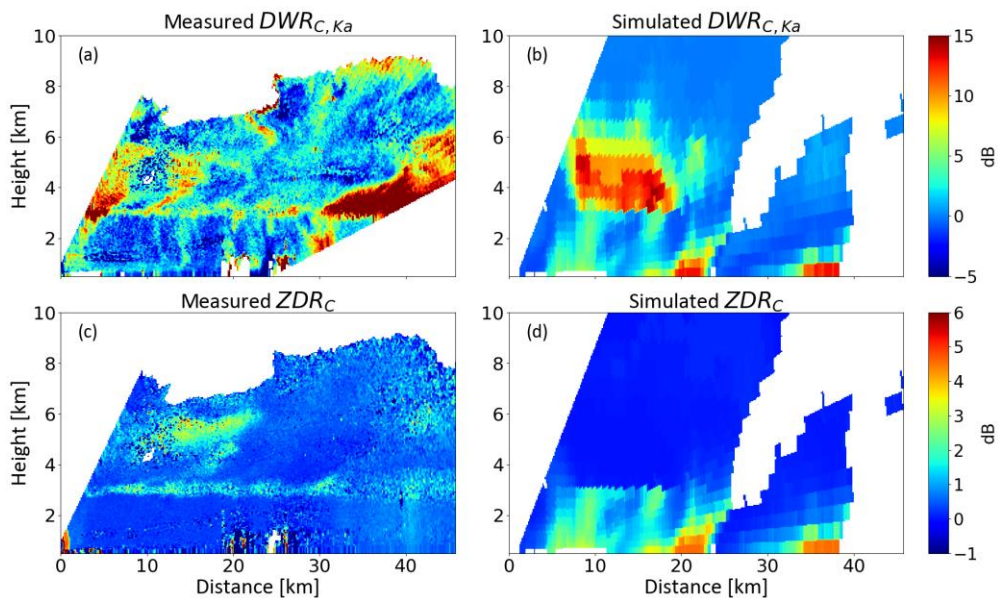
918

919

920

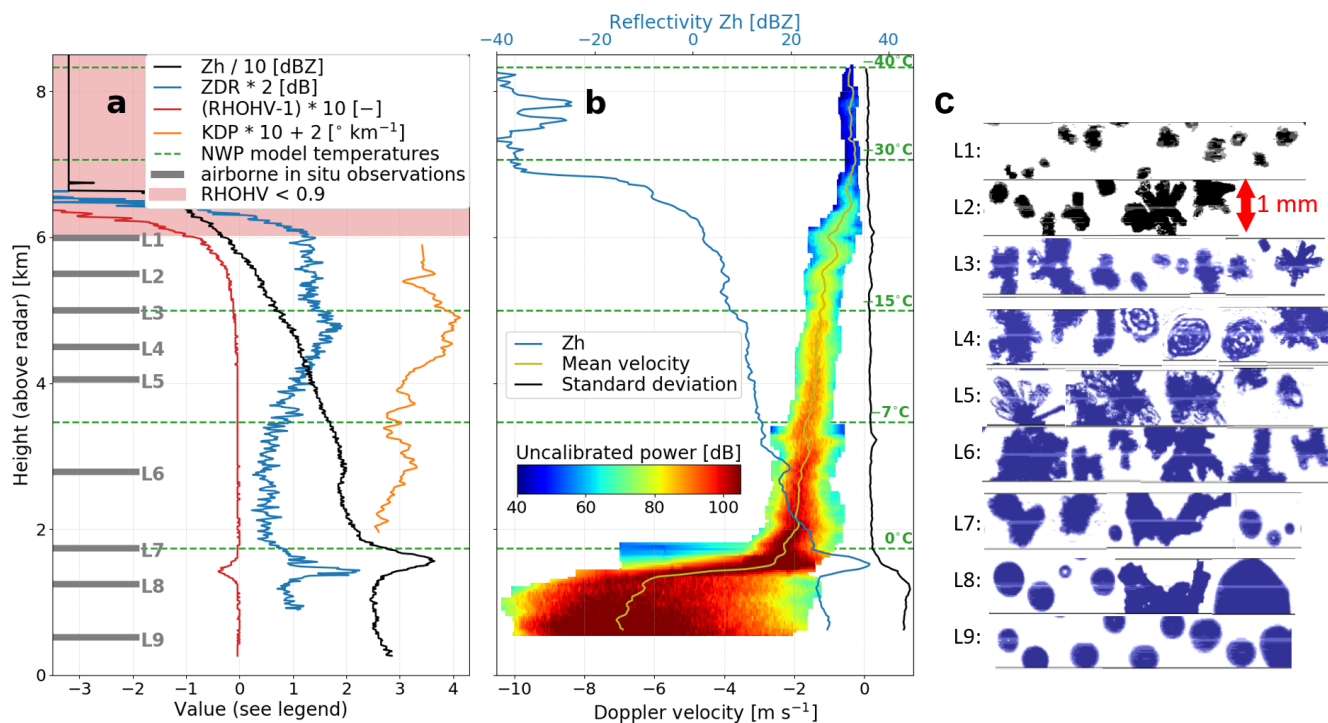
921

922



923

924 **Figure 2** (a) Dual-wavelength ratio between the C-band POLDIRAD and Ka-band miraMACS measurements on the 7th July 2019,
 925 (b) Differential radar reflectivity Z_{DR} measured by the C-band radar POLDIRAD, (c) Simulated dual-wavelength ratio and (d)
 926 simulated Z_{DR} of a comparable, but not identical, precipitation event using the P3 scheme (Morrison and Milbrandt, 2015).

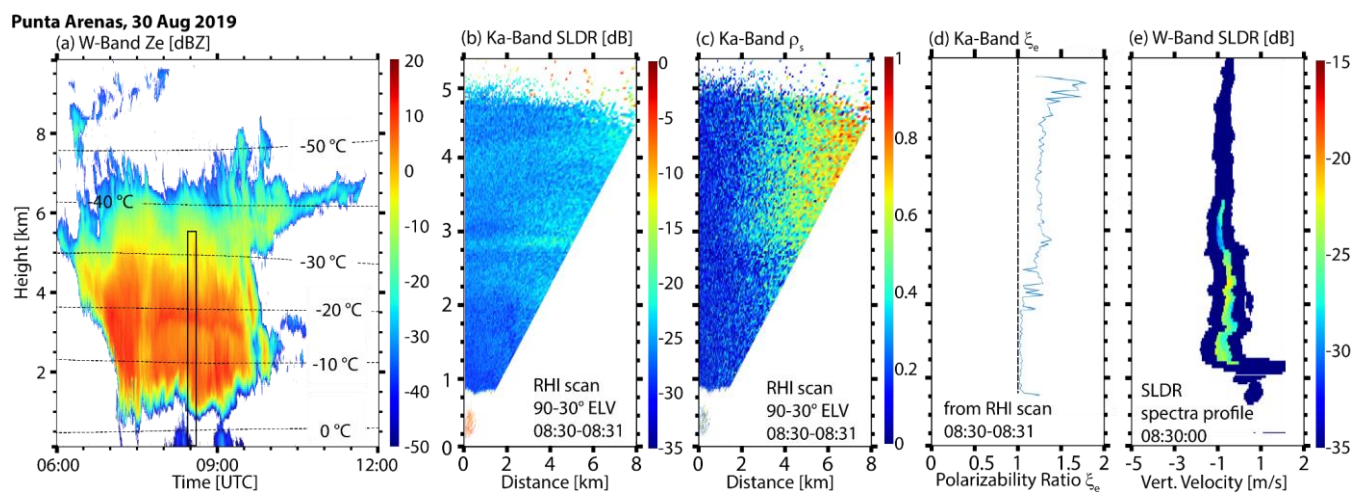


927



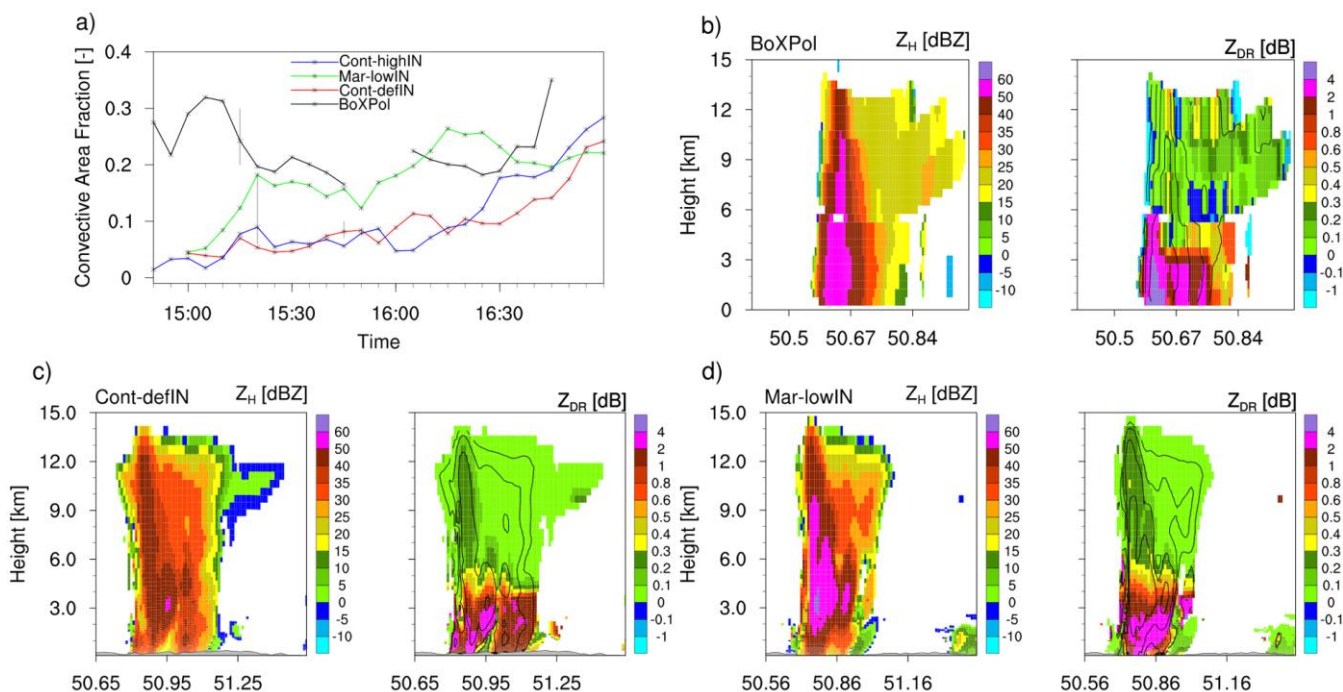
928 **Figure 3:** Measurements of slant-viewing and zenith-pointing polarimetric C-band weather radar scans with NWP model based
 929 temperature levels and airborne in-situ observations: (a) quasi-vertical profiles (QVPs) of radar reflectivity Z_H , differential
 930 reflectivity Z_{DR} , copolar cross-channel correlation coefficient ρ_{HV} , and the specific differential phase K_{DP} estimated from (noisy)
 931 measurements of the differential phase by aggressive filtering above the melting layer; (b) average Doppler spectra from a 15 s
 932 birdbath scan and corresponding first 3 moments at each radar bin height: reflectivity, power-weighted mean velocity and standard
 933 deviation; (c) in situ particle images (downward-looking projection images) collected at altitudes L1 to L9.

934
 935
 936
 937



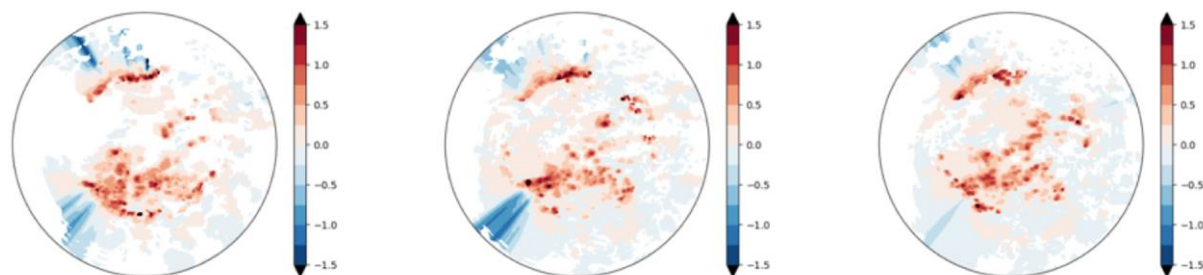
938 **Figure 4:** Case study of a deep mixed-phase cloud event observed with multiwavelength polarimetric cloud radars at Punta Arenas,
 939 Chile, on 30 August 2019. (a) vertical-stare W-Band (94-GHz) radar reflectivity factor Z_e and isolines of modelled air temperature,
 940 (b) and (c) Ka-Band (35-GHz) RHI scans (90°-30° elevation) of slanted linear depolarization ratio SLDR and co-cross correlation
 941 coefficient in the slanted basis ρ_s , respectively, from 08:30-08:31 UTC, (d) profile of the shape index polarizability ratio (ξ_e) obtained
 942 from the RHI scans shown in (b) and (c), and (e) height spectrogram (at 90° elevation) of W-Band SLDR from 08:30:00 UTC. The
 943 time and height frame of panels (b-e) is indicated by the black rectangle in (a).
 944

945



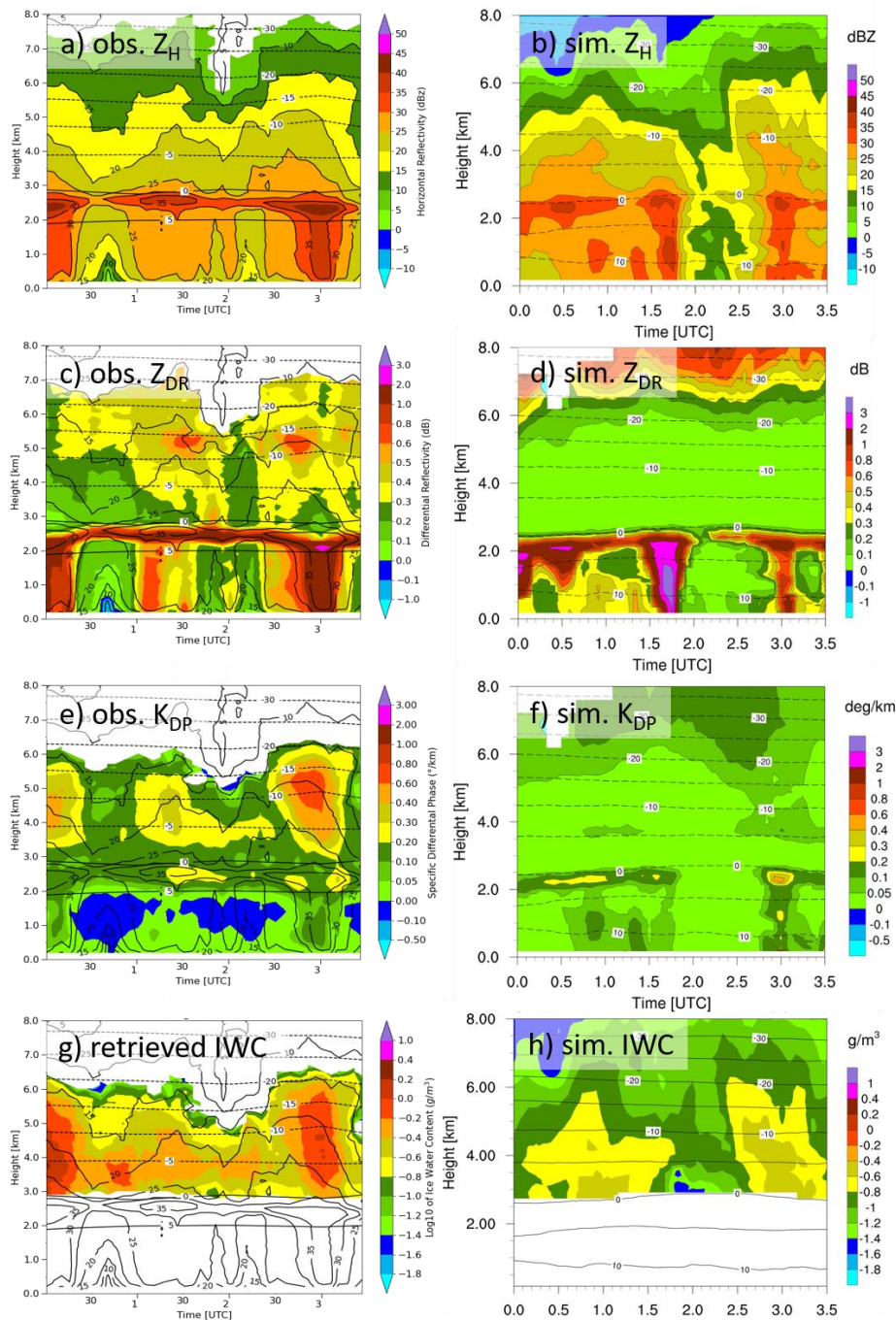
946
 947 **Figure 5: Time-series of Convective Area Fraction (CAF) evolution (panel a) and reconstructed observed (panel b) and**
 948 **simulated/synthetic range-height-indicators (RHI) of horizontal reflectivity Z_H and differential reflectivity Z_{DR} (panels c and d).**
 949 **Synthetic RHIs are based on simulations for actual land-cover with different perturbations of CN and IN concentrations, where**
 950 **Cont-defIN indicates continental aerosol with default IN concentration and Mar-lowIN indicates maritime aerosol with low IN**
 951 **concentration. The gaps in the BoXPol-observed CAF time series are due to strong attenuation.**

952



953

954 **Figure 6: Synthetic PPI of Z_{DR} at 0.5 deg elevation for the DWD radar site Neuheilenbach based on the analysis obtained for June**
 955 **4 at 16:00 UTC by assimilation of radar reflectivity and using three different ways to specify the model error: large scale uncertainty**
 956 **(left), large plus unresolved scales uncertainty (middle) and in addition the use of the warm bubble approach (right).**



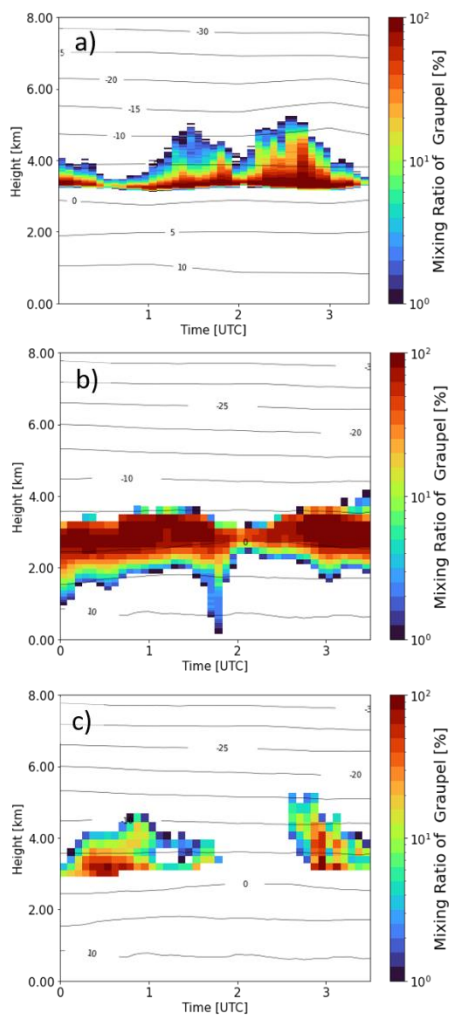
957

958 **Figure 7: Quasi-vertical profiles (QVPs) of observed (left column) and imulated polarimetric radar variables (right column), i.e.**
959 **horizontal reflectivity Z_H (panels a and b), differential reflectivity Z_{DR} (panels c and d), specific differential phase K_{DP} (panels e and**
960 **f), together radar-retrieved ice water content (IWC, panel g) and simulated IWC (panel h). The QVPs show a stratiform rain event**



961 observed on 7 October 2014 between 0 and 3:30 UTC with the polarimetric X-band radar in Bonn, BoXPoL, and simulated with
962 COSMO version 5.1 and the 2-moment cloud microphysics scheme.

963



964

965 **Figure 8: Retrieved and simulated graupel mixing ratios, defined as the percentage of graupel in the total hydrometeor mass, for**
966 **the stratiform rain event shown in Fig. 7 (7 October 2014, 0-3:30 UTC). An advanced hydrometeor classification and quantification**
967 **algorithm has been applied to polarimetric BoXPoL measurement (panel a) and to simulated radar variables based on COSMO**
968 **simulations (panel c) and compared to the COSMO-simulated graupel mixing (panel b).**

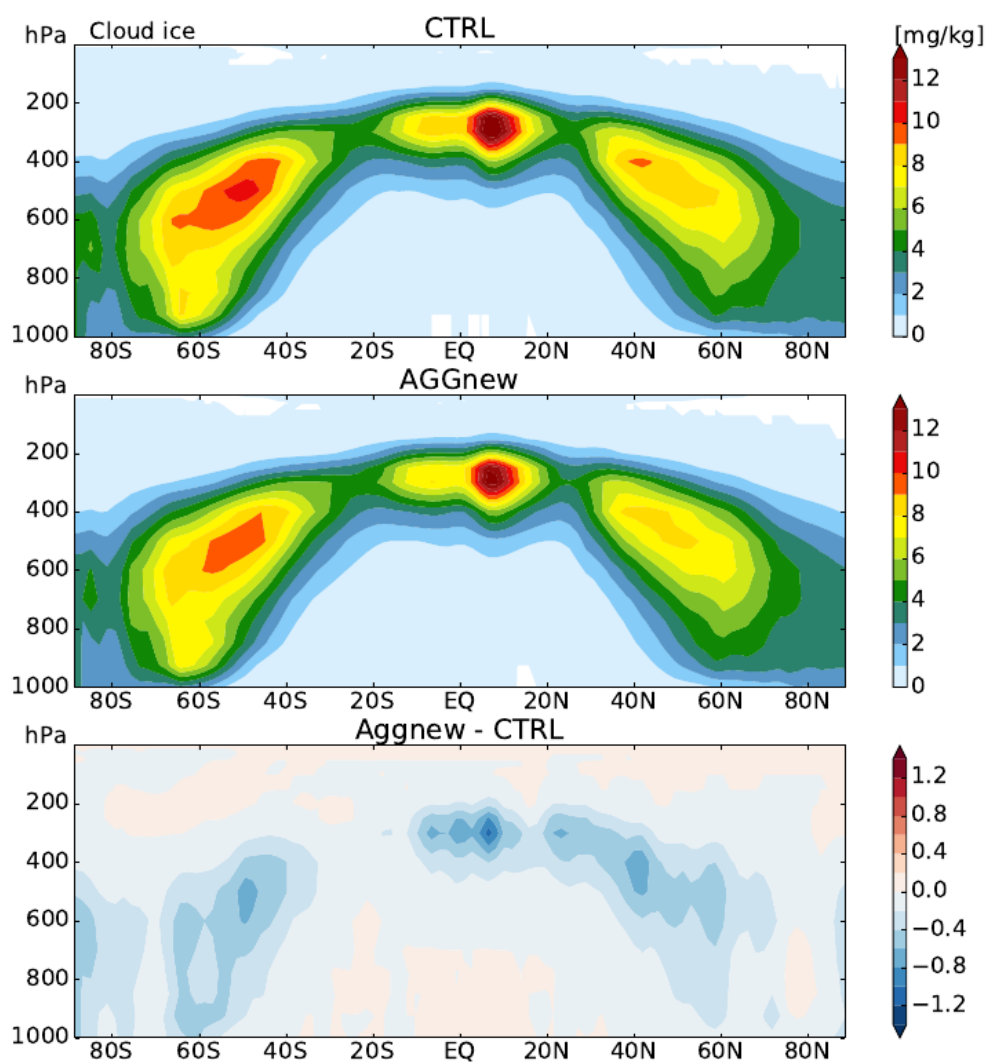
969

970



971

972



973

974 **Figure 9:** Specific ice water, q_i , [g kg^{-1}] as zonal, annual mean for (top) standard ICON GCM output, (middle) aggregation
975 parameterization revised as stochastic parameterization drawing from the q_i subgrid-variability PDF, and (bottom) difference
976 between the two.

977

978